Department of Mathematics and Statistics
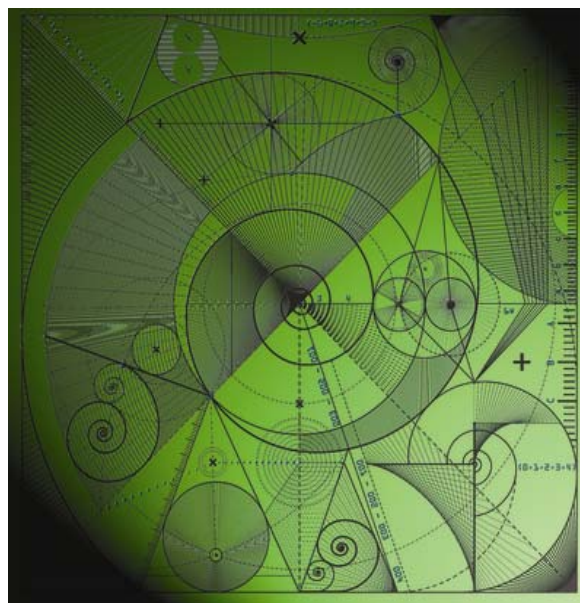
28 January 2013

Hybrid numerical-asymptotic approximation for high frequency scattering by penetrable convex polygons

by

Samuel P. Groth, David P. Hewett and
Stephen Langdon

Hybrid numerical-asymptotic approximation for high frequency scattering by penetrable convex polygons

SAMUEL P. GROTH, DAVID P. HEWETT AND STEPHEN LANGDON

Department of Mathematics and Statistics, University of Reading,

Whiteknights PO Box 220, Reading, RG6 6AX, UK.

Abstract: We consider time-harmonic scattering by penetrable convex polygons, a Helmholtz transmission problem. Standard numerical schemes based on piecewise polynomial approximation spaces become impractical at high frequencies due to the requirement that the number of degrees of freedom in any approximation must grow at least linearly with respect to frequency in order to represent the oscillatory solution. High frequency asymptotic methods on the other hand are non-convergent and may be insufficiently accurate at low to medium frequencies. Here, we design a hybrid numerical-asymptotic boundary element approximation space that combines the best features of both approaches. Specifically, we compute the classical geometrical optics solution using a beam tracing algorithm, and then we approximate the remaining diffracted field using an approximation space enriched with carefully chosen oscillatory basis functions. We demonstrate via numerical simulations that this approach permits the accurate and efficient representation of the boundary solution and the far field pattern.

Keywords: Helmholtz transmission problem, high frequency scattering, numerical-asymptotic approximation, boundary integral equation method

1 Introduction

The scattering and absorption of time-harmonic electromagnetic and acoustic waves by penetrable (i.e. partially transparent) scatterers arises in numerous applications of mathematical and physical interest, for example the scattering of light waves by atmospheric particles such as ice crystals and aerosols (see, e.g., Baran (2012)). When both the penetrable scatterer and the exterior medium of propagation are homogeneous, a natural approach is to reformulate the problem as a system of integral equations that hold on the boundary of the scatterer. This replaces a problem on an unbounded domain with one on a bounded domain of reduced dimension. The study of boundary integral equation (BIE) formulations for such problems, and their numerical solution (the Boundary Element Method (BEM), often called the Method Of Moments in the electromagnetic community), has a long history. Single smooth penetrable scatterers have been studied by, e.g., Kress & Roach (1978), Kleinman & Martin (1988), Zinn (1989), Rapún & Sayas (2006), Domínguez et al. (2008), Hsiao & Xu (2011), Kleefeld (2012), whilst Costabel & Stephan (1985) considered both smooth and polygonal scatterers, and Torres & Welland (1993), Rapún & Sayas (2008), Laliena et al. (2009), von Petersdorff (1989) and Hiptmair & Jerez-Hanckes (2012) have considered Lipschitz domains, the latter two describing formulations for multiple penetrable scatterers.

All of the numerical approaches listed above suffer however from the well known limitation (common to all conventional numerical methods for wave scattering simulations implemented using piecewise polynomial approximation spaces) that a fixed number of degrees of freedom is required per wavelength in order to represent the oscillatory solution. This can lead to prohibitive computational expense when the scatterer is large relative to the wavelength, as is often the case in applications. In this "high frequency" regime one can alternatively appeal to asymptotic approximation techniques such as Geometrical Optics (GO), Physical Optics (PO, sometimes called the "Kirchoff approximation") and the Geometrical Theory of Diffraction (GTD). However, although such approximations have a low (in fact, often frequency-independent) computational cost, the price one pays is that they are only accurate for "sufficiently high" frequencies. The question of how high the frequency needs to be for "sufficient accuracy" depends on the particular scattering problem being considered, and moreover is usually not known a priori. In many applications (in particular for the example of light scattering by atmospheric particles mentioned above) there is a significant and important range of frequencies for which

neither conventional numerical methods nor asymptotic methods give satisfactory results.

The *hybrid numerical-asymptotic* (HNA) approach is a general methodology for scattering problems which aims to fuse conventional numerical methods with high frequency asymptotics to create algorithms that are controllably accurate and computationally feasible over the whole frequency range. The key idea is to enrich the BEM approximation space with oscillatory functions, chosen using partial knowledge of the high frequency asymptotic behaviour of the solution. More explicitly, one seeks to approximate the unknown solution v of the relevant BIE using an ansatz of the form

$$v(\mathbf{x},k) \approx v_0(\mathbf{x},k) + \sum_{m=1}^{M} v_m(\mathbf{x},k) \exp(ik\psi_m(\mathbf{x})), \quad \mathbf{x} \in \Gamma, \tag{1.1}$$

where k (the wavenumber) is proportional to the frequency of the waves, and Γ is the boundary of the scatterer. In this representation, v_0 is a known (generally oscillatory) function (derived from the high frequency asymptotics), the phases ψ_m are chosen a priori (again, using the high frequency asymptotics) and the amplitudes v_m, $m = 1, \ldots, M$, are approximated numerically using piecewise polynomials. The expectation is that if v_0 and ψ_m, $m = 1, \ldots, M$, are chosen wisely, then $v_m(\cdot, k)$, $m = 1, \ldots, M$, will be much less oscillatory than $v(\cdot, k)$ and so can be more efficiently approximated by piecewise polynomials than v itself.

For a number of important classes of scattering problems the HNA approach has been shown to provide a dramatic reduction in the number of degrees of freedom required at high frequencies compared to conventional methods. However, to date the HNA approach appears to have been applied exclusively to problems of scattering by *impenetrable* scatterers, i.e. where perfectly-conducting, sound-soft (Dirichlet), sound-hard (Neumann) or impedance (Robin) boundary conditions are imposed on the boundary Γ. Moreover, until very recently (Chandler-Wilde et al., 2012b), its successful application was restricted to convex impenetrable scatterers, for which multiple re-reflections and questions of partial illumination need not be considered. For a comprehensive historical and technical review of the HNA approach in the BEM setting the reader is referred to Chandler-Wilde et al. (2012a).

The purpose of the current paper is to begin the challenging task of generalising the HNA methodology to the case of so-called "transmission problems" for *penetrable* scatterers, where the scatterer is a region in which the wave speed differs from that of the background propagation medium. Specifically, we consider the two-dimensional case where the scattering region is bounded by a convex polygon. We also consider the possibility that the interior medium may be absorbing. For an illustration of a typical solution see Figure 1. Our aim is to

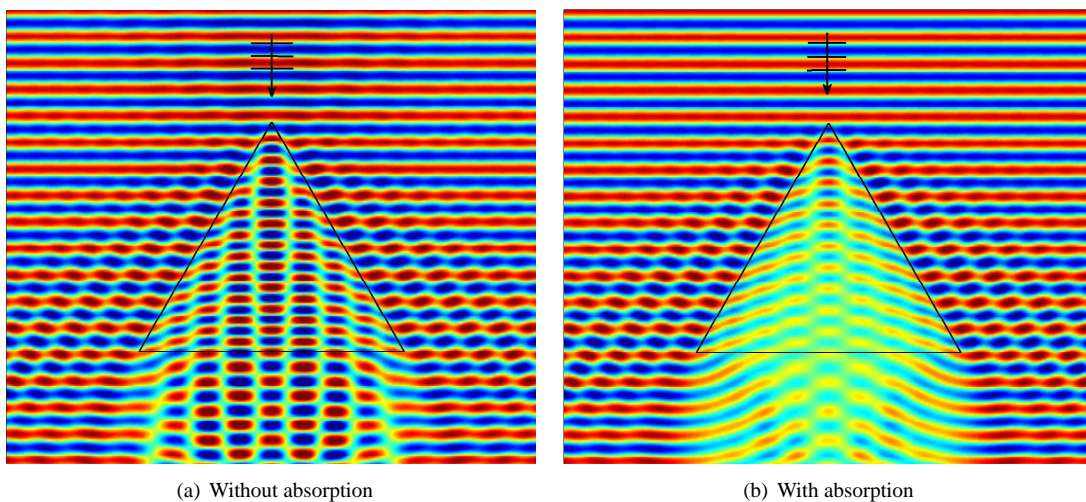(a) Without absorption   (b) With absorption

FIG. 1: Real part of the total field for scattering of a plane wave by a penetrable equilateral triangle. Details of the parameter values used in these examples are given in §4.

show how effective HNA approximation spaces can be constructed for this problem, and moreover to demon-

strate, by comparison with an "exact" reference solution (computed using a conventional BEM with a large number of degrees of freedom), that these HNA approximation spaces can approximate the highly oscillatory solution of the transmission problem accurately and efficiently, even at high frequencies. The development of an HNA BEM based on these approximation spaces will be reported separately (Groth et al., 2013).

The main difficulty in the generalisation of the HNA methodology to the penetrable case is that the high frequency asymptotic behaviour is significantly more complicated than in the impenetrable case. In particular, the boundary of the scatterer represents the interface between two media with different wave speeds, and hence two different wavenumbers, and we expect to need to modify the ansatz (1.1) to include terms oscillating at both wavenumbers. In addition to the phenomena of reflection and diffraction that occur in the impenetrable case, in the penetrable case we observe a new phenomenon, *refraction*, which occurs when a wave propagating in the exterior medium is transmitted into the scatterer and vice versa. One key difficulty this presents is that a wave propagating inside the scatterer can undergo multiple (in fact, infinitely many) internal reflections/diffractions (this is described in more detail in §3). We therefore expect that, in order for v_m, $m = 1, 2, \ldots$, to be non-oscillatory, we would need to consider infinitely many different phases ψ_m. (This is in contrast to the case of scattering by sound-soft convex polygons considered in Chandler-Wilde & Langdon (2007) and Hewett et al. (2012), where the high frequency behaviour can be completely captured using just two phase functions, i.e. $M = 2$ in (1.1), corresponding to waves travelling clockwise and anticlockwise around the boundary.) This complicates the development of an ansatz of the form (1.1) for the transmission problem, because to create a viable numerical algorithm we have to choose only a finite number of these phases. Depending on the refractive index (the ratio of the interior to exterior wavenumbers), at each reflection/diffraction the amplitude of the reflected wave decreases, and hence, as we will see in §4, truncating a series of re-reflections/re-diffractions after a few terms (i.e. including only a small number of phases) is often sufficient to achieve an excellent approximation of the true solution.

Moreover, the higher the absorption of the interior medium, the faster the decay of the amplitude of waves passing through the scatterer, and, as a result, our HNA approximation spaces are more accurate at higher absorptions, as we will see in §4. Indeed, for high absorption in the scatterer, a transmission problem can be approximated by an appropriate exterior problem with impedance boundary condition (see, e.g., Antoine & Barucq (2005) or Haddar et al. (2005) for details). The effectiveness of the HNA approach for scattering by convex polygons with impedance boundary conditions was demonstrated in Chandler-Wilde et al. (2012c), where it was shown that an approximation space could be constructed for which the number of degrees of freedom required to achieve a prescribed level of accuracy for the best approximation grew only logarithmically with respect to frequency (compared to at least linear growth for conventional approximation spaces). Thus the HNA approach has been shown to work well for the transmission problem in the high absorption limit, with our current paper focusing on extending those ideas to general absorptions and frequencies.

Another key difficulty is that the high frequency asymptotic theory for penetrable scatterers is not nearly as well understood as for the impenetrable case. In particular, there is no known closed-form analytical (or even asymptotic) solution to the canonical problem of diffraction by a penetrable wedge, despite many attempts to derive one (see, e.g., Meister et al. (1994), Rawlins (1999), Budaev & Bogy (1999), Antipov & Silvestrov (2007)). This means that we do not have a fully-developed GTD for penetrable scatterers from which to infer the correct choice of phases ψ_m in our HNA ansatz (1.1). Our approach in this paper chooses phase functions based on heuristic generalisations of the asymptotic theory (GO and GTD) for the impenetrable case, and confirms the validity of these choices via a series of numerical examples. In contrast to classical asymptotics, we do not seek a complete representation of the high frequency behaviour of the solution, rather we just seek information about the phase; this enables the construction of our hybrid numerical-asymptotic approximation space, with the non-oscillatory amplitudes (v_m in (1.1)) being approximated by standard piecewise polynomials on appropriately graded meshes.

Problems of the type considered in this paper have been studied widely in the electromagnetics community, where the state of the art in computational methods grounded in high frequency asymptotics appears to be the so-called physical-geometric optics hybrid (PGOH) method detailed in Bi et al. (2011) (building on earlier work in Yang & Liou (1995, 1996, 1997)). The PGOH approach is essentially a generalised PO (or Kirchoff) approximation, being based on the classical boundary integral representation formula for the solution of the scattering problem (cf. (2.6)-(2.7) below), with the (unknown) Cauchy data being replaced by its GO approxi-

mation. This corresponds to using only the term v_0 in the ansatz (1.1) (or more accurately the term v_{go} in the generalised ansatz (3.1)–(3.2) which we introduce in §3). Our approach is considerably more ambitious, in that our HNA approximation space (through the inclusion of the other terms in (1.1) (corresponding to v_d in (3.1))) also captures diffraction effects directly in the approximation of the boundary solution. A result is that, whereas the PGOH approach is limited to high frequency (and cannot offer controllable accuracy for fixed frequency), our approximation space is effective across the frequency spectrum (see §4).

An outline of the paper is as follows. We begin in §2 by stating precisely the scattering problem to be solved and detailing its reformulation as a boundary integral equation. In §3 we describe our HNA approximation. The first step is to compute the GO approximation, i.e. the leading order term v_0 in (1.1), and we describe our approach (a beam tracing algorithm) for doing this for a convex polygonal scatterer of arbitrary absorption in §3.1. A key ingredient of the algorithm is the solution of the canonical problem of scattering of an incident plane wave by a planar interface between two absorbing media of different wavenumbers. This classical problem has been studied by a number of authors (see, e.g., Dupertuis et al. (1994), Chang et al. (2005), Yang & Liou (2009)) but there does not seem to be a definitive reference suitable for our purposes. Indeed, we believe that Chang et al. (2005) and Yang & Liou (2009) contain fundamental errors in certain formulae, and Dupertuis et al. (1994) does not provide a complete prescription of how to make various important sign choices. We therefore provide a complete derivation of the solution to this problem in the appendix.

In §3.2 we discuss how ideas from the GTD can be used to understand the oscillatory behaviour of the diffracted field in the penetrable scatterer, and we use this knowledge to inform our choice of the phases ψ_m in (1.1). We present two different levels of approximation, first just considering the effect of diffraction from corners of the polygon onto adjacent sides ("Approximation Space 1", described in §3.2.2), and then including the higher order effect (in the sense of high frequency asymptotics) of diffraction from corners onto non-adjacent sides ("Approximation Space 2", described in §3.2.3). We put these approximation spaces to the test in §4, by performing a least squares fit to a reference solution obtained using a standard BEM. The results of this fit for different levels of absorption and a range of wavenumbers suggest that, compared to GO, a significant improvement in accuracy can be achieved with a very modest number of degrees of freedom. Moreover, for a fixed number of degrees of freedom the relative error in our best approximation does not grow significantly as frequency increases.

2 Problem statement

We consider the two-dimensional problem of scattering of a time-harmonic incident plane wave

$$u^i(\mathbf{x}) := \mathrm{e}^{ik_1 \mathbf{d}^i \cdot \mathbf{x}} \tag{2.1}$$

by a penetrable convex polygon. Here $k_1 > 0$ is the wavenumber in the medium surrounding the polygon, $\mathbf{x} = (x_1, x_2) \in \mathbb{R}^2$, and $\mathbf{d}^i \in \mathbb{R}^2$ is a unit direction vector. Let Ω_2 denote the interior of the polygon, let $\Omega_1 := \mathbb{R}^2 \backslash \overline{\Omega_2}$ denote the exterior unbounded domain, and let $\Gamma = \Gamma_1 \cup \Gamma_2 \cup \ldots \Gamma_{n_s}$ denote the boundary of the polygon where n_s is the number of sides and Γ_j, $j = 1, \ldots, n_s$, are the sides of the polygon, which we label in an anticlockwise direction. The corners of the polygon are similarly labelled $\mathbf{P}_1, \ldots, \mathbf{P}_{n_s}$, with Γ_j, $j = 1, \ldots, n_s$, being the side between the corners $\mathbf{P}_j$ and $\mathbf{P}_{j+1}$ (with the convention $\mathbf{P}_{n_s+1} \equiv \mathbf{P}_1$). The boundary value problem (BVP) we wish to solve is: given the incident field u^i, determine the total field u_1 in Ω_1 and u_2 in Ω_2 such that, with k_2 denoting the wavenumber inside the polygon and $\mathbf{n}$ denoting the outward unit normal to Γ,

$$\Delta u_1 + k_1^2 u_1 = 0, \quad \text{in } \Omega_1, \tag{2.2}$$

$$\Delta u_2 + k_2^2 u_2 = 0, \quad \text{in } \Omega_2, \tag{2.3}$$

$$u_1 = u_2 \text{ and } \frac{\partial u_1}{\partial \mathbf{n}} = \frac{\partial u_2}{\partial \mathbf{n}}, \quad \text{on } \Gamma, \tag{2.4}$$

and the *scattered field* $u^s := u_1 - u^i$ satisfies the *Sommerfeld radiation condition*, that

$$\frac{\partial u^s}{\partial r}(\mathbf{x}) - ik_1 u^s(\mathbf{x}) = o(r^{-1/2}), \quad \text{as } r := |\mathbf{x}| \to \infty. \tag{2.5}$$

We shall assume throughout that $k_1 > 0$ and that $k_2 \in \mathbb{C}$, with $\mathrm{Re}\,[k_2] > 0$ and $\mathrm{Im}\,[k_2] \geqslant 0$; when $\mathrm{Im}\,[k_2] > 0$ the scatterer is partially absorbing. The unique solvability of this BVP is well known (see, e.g., Laliena et al. (2009, Proposition 2.1 and Corollary 3.4), which follows from results in Costabel & Stephan (1985) and Torres & Welland (1993), and also the related result Marmolejo-Olea et al. (2012, Corollary 8.5)).

Now we state a BIE formulation for (2.2)–(2.5). Note that, in this paper, we only actually solve this BIE (using a standard hp-BEM) in order to compute reference solutions for our examples in §4. The main reason for including this here is as a motivation for why we want to understand the approximation properties of the boundary solution (as mentioned in §1, we will describe a BEM based on the HNA approximation space proposed in this paper in Groth et al. (2013)). If u_1 and u_2 satisfy the BVP, then a form of Green's representation theorem holds, namely (cf., e.g., Chandler-Wilde et al. (2012a, Theorems 2.20 and 2.21))

$$u_1(\mathbf{x}) = u^i(\mathbf{x}) + \int_\Gamma \left(u_1(\mathbf{y}) \frac{\partial \Phi_1(\mathbf{x},\mathbf{y})}{\partial \mathbf{n}(\mathbf{y})} - \Phi_1(\mathbf{x},\mathbf{y}) \frac{\partial u_1(\mathbf{y})}{\partial \mathbf{n}(\mathbf{y})} \right) \mathrm{d}s(\mathbf{y}), \quad \mathbf{x} \in \Omega_1, \tag{2.6}$$

$$u_2(\mathbf{x}) = \int_\Gamma \left(\Phi_2(\mathbf{x},\mathbf{y}) \frac{\partial u_2(\mathbf{x})}{\partial \mathbf{n}(\mathbf{y})} - u_2(\mathbf{y}) \frac{\partial \Phi_2(\mathbf{x},\mathbf{y})}{\partial \mathbf{n}(\mathbf{y})} \right) \mathrm{d}s(\mathbf{y}), \quad \mathbf{x} \in \Omega_2, \tag{2.7}$$

where $\Phi_j(\mathbf{x},\mathbf{y}) := (\mathrm{i}/4) H_0^{(1)}(k_j |\mathbf{x}-\mathbf{y}|)$, $j = 1,2$, are the fundamental solutions of the Helmholtz equations (2.2) and (2.3), respectively, with $H_\nu^{(1)}$ denoting the Hankel function of the first kind of order ν. Henceforth we shall denote u_1 and u_2 on Γ simply by u since $u_1 = u_2$ on Γ and, similarly, $\partial u_1/\partial \mathbf{n}$ and $\partial u_2/\partial \mathbf{n}$ on Γ will be denoted simply by $\partial u/\partial \mathbf{n}$.

Using the standard jump relations for layer potentials (cf. Chandler-Wilde et al. (2012a, p.115)) it follows that the unknown boundary data $v := (u, \partial u/\partial \mathbf{n})$ satisfies the following BIE:

$$Av = f, \tag{2.8}$$

where

$$A = \begin{pmatrix} I + D_2 - D_1 & S_1 - S_2 \\ H_2 - H_1 & I + D'_1 - D'_2 \end{pmatrix}, \qquad f = \begin{pmatrix} u^i \\ \partial u^i/\partial \mathbf{n} \end{pmatrix}.$$

Here I is the identity operator and S_j, D_j, D'_j, H_j, for $j = 1,2$, are, respectively, the single-layer, double-layer, adjoint double-layer and hypersingular integral operators defined for $\phi \in L^2(\Gamma)$ by

$$S_j \phi(\mathbf{x}) := \int_\Gamma \Phi_j(\mathbf{x},\mathbf{y}) \phi(\mathbf{y}) \mathrm{d}s(\mathbf{y}), \qquad D_j \phi(\mathbf{x}) := \int_\Gamma \frac{\partial \Phi_j(\mathbf{x},\mathbf{y})}{\partial \mathbf{n}(\mathbf{y})} \phi(\mathbf{y}) \mathrm{d}s(\mathbf{y}),$$

$$D'_j \phi(\mathbf{x}) := \int_\Gamma \frac{\partial \Phi_j(\mathbf{x},\mathbf{y})}{\partial \mathbf{n}(\mathbf{x})} \phi(\mathbf{y}) \mathrm{d}s(\mathbf{y}), \quad H_j \phi(\mathbf{x}) := \frac{\partial}{\partial \mathbf{n}(\mathbf{x})} \int_\Gamma \frac{\partial \Phi_j(\mathbf{x},\mathbf{y})}{\partial \mathbf{n}(\mathbf{y})} \phi(\mathbf{y}) \mathrm{d}s(\mathbf{y}).$$

Our BIE (2.8) is similar to that in Colton & Kress (1983, §3.8) (where only smooth scatterers are considered), and also to that proposed in Torres & Welland (1993) (albeit for an indirect method, in which the unknowns are non-physical "densities", rather than the boundary data itself). By the well-known mapping properties of the integral operators (cf., e.g., Chandler-Wilde et al. (2012a, Theorems 2.17 and 2.18)),

$$A : H^{s+1/2}(\Gamma) \times H^{s-1/2}(\Gamma) \to H^{s+1/2}(\Gamma) \times H^{s-1/2}(\Gamma)$$

is a bounded operator for all $-1/2 \leqslant s \leqslant 1/2$. In particular, $A : H^1(\Gamma) \times L^2(\Gamma) \to H^1(\Gamma) \times L^2(\Gamma)$ is bounded. But also $A : L^2(\Gamma) \times L^2(\Gamma) \to L^2(\Gamma) \times L^2(\Gamma)$ is bounded because the difference $H_2 - H_1$ is bounded (in fact, compact) from $L^2(\Gamma)$ to $L^2(\Gamma)$ (see, e.g., Torres & Welland (1993, Lemma 6.2(vi))).

Whereas for the general transmission BVP we would only have that the trace of u was in $H^{1/2}(\Gamma)$ and $\partial u/\partial \mathbf{n}$ in $H^{-1/2}(\Gamma)$, here the extra smoothness of the solution follows from the smoothness of the incident plane wave (this is analogous to the case of a bounded impenetrable scatterer, see Chandler-Wilde et al. (2012a, Theorem 2.12)). Specifically, it follows from (2.1) that $f \in H^1(\Gamma) \times L^2(\Gamma)$. The invertibility of A from $H^1(\Gamma) \times L^2(\Gamma) \to H^1(\Gamma) \times L^2(\Gamma)$ follows from a modification of the argument in Torres & Welland (1993, Proof of Theorem 7.2) and hence the solution v of (2.8) is in $H^1(\Gamma) \times L^2(\Gamma)$, and hence in $L^2(\Gamma) \times L^2(\Gamma)$. This is the setting in which we work in this paper.

We remark that other BIE formulations of the transmission problem are also possible - see, e.g., Costabel & Stephan (1985), Rapún & Sayas (2008), Laliena et al. (2009), Hsiao & Xu (2011). Moreover, the approximation results we derive in the following sections are equally relevant for any direct BIE formulation, not just the particular one (2.8) described above.

3 Hybrid numerical-asymptotic approximation space

Our proposed high frequency HNA approximation space for the unknown $v = (u, \partial u / \partial \mathbf{n})$ in the BIE (2.8) is constructed in two stages. First we decompose

$$v(\mathbf{x}) = v_{go}(\mathbf{x}) + v_d(\mathbf{x}), \qquad \mathbf{x} \in \Gamma, \tag{3.1}$$

where $v_{go} = (u_{go}, \partial u_{go} / \partial \mathbf{n})$ is the GO approximation to v, with the remainder $v_d = (u_d, \partial u_d / \partial \mathbf{n})$ being interpreted as the diffracted field. The GO approximation v_{go} represents the leading-order behaviour at high frequencies, and takes into account the basic GO phenomena of reflection and refraction by the edges of the polygon. It can be computed analytically using a beam-tracing algorithm, which we describe in more detail in §3.1. It is v_{go} which we take as our known leading order behaviour v_0 in (1.1). Second, we aim to approximate the remaining diffracted field v_d using an ansatz of the form

$$v_d(\mathbf{x}) \approx \sum_{m=1}^{M_1} v_{1,m}(\mathbf{x}, k_1) \exp(\mathrm{i} k_1 \psi_{1,m}(\mathbf{x})) + \sum_{m=1}^{M_2} v_{2,m}(\mathbf{x}, k_2) \exp(\mathrm{i} k_2 \psi_{2,m}(\mathbf{x})), \tag{3.2}$$

which generalises the standard HNA ansatz (1.1) to the case where two different wavenumbers are present. As will be discussed in §3.2, the phases $\psi_{j,m}$, $j = 1, 2$, will be chosen based on heuristic high frequency asymptotics, and the amplitudes $v_{j,m}$, $j = 1, 2$, will be approximated numerically by piecewise polynomials on appropriately graded meshes. The efficacy of our proposed approximation spaces will be demonstrated in §4.

3.1 *Geometrical optics approximation v_{go}*

In the GO approximation, a ray from the incident field striking a point on a smooth portion of the boundary Γ gives rise to a *reflected* ray propagating back into the exterior domain Ω_1 and a *refracted* ray, propagating into the interior of the polygon Ω_2. Since we assume that Ω_2 is convex, the reflected ray propagates away to infinity without re-intersecting the boundary Γ. The refracted (or *transmitted*) ray, on the other hand, does re-intersect Γ, and if this intersection occurs on a smooth portion of Γ then further reflection/refraction occurs, with a refracted ray propagating out of the polygon into the exterior domain and an internally-reflected ray propagating back into the polygon. This internally-reflected ray can, in turn, be re-reflected/refracted, and this process continues indefinitely, giving an infinite number of internally-reflected rays, potentially all propagating in different directions.

The directions of the reflected/refracted rays and the amplitudes/phases of the fields propagating along them are governed by the well-known laws of reflection and refraction for a plane wave incident on an infinite transmission interface (i.e. the Fresnel formulae and Snell's Law). However, although these laws are completely classical in the case when both propagation media are non-absorbing (see, e.g., Born & Wolf (1997)), the generalisation to the case where one or more of the media are absorbing seems to have generated a certain amount of confusion in the literature. As explained in §1, for completeness and to correct some mistakes in earlier works we provide a full derivation of the reflection/refraction laws in the general case of transmission between two absorbing media in Appendix A.

A number of numerical algorithms have been presented for computing the GO approximation for the transmission problem using the Fresnel formulae and Snell's law (see, e.g., Yang & Liou (1995), where the 2D problem of this paper is considered, and also Bi et al. (2011) and Macke et al. (1996), where a 3D analogue is studied). Many such algorithms (in particular, Yang & Liou (1995) and Macke et al. (1996)) adopt a ray-based approach in which the incident wave is discretised into a large number of rays, each of which are traced individually as they reflect/refract within the scatterer, with the algorithm stopping after a certain (user-specified) number of internal reflections. This approach is general, in that it can be applied to smooth scatterers as well as

to polygons/polyhedra. For polygons/polyhedra, however, the fact that the boundary Γ is composed of straight sides/faces means that the GO approximation consists of a collection of *beams* of rays propagating in the same direction and with the same amplitude. Each beam can be thought of as a plane wave with an associated propagation direction and amplitude, restricted to a certain subset of $\mathbb{R}^2$. As a result, one does not need to discretise the incident wave into a large number of rays; rather, one need only compute the propagation direction and amplitude of the plane wave associated with each beam, and record the position of the "limiting rays" which form the edges of the beam. Once the algorithm has been run once for a given geometry and incident direction, the GO approximation v_{go} is then readily computed at any observation point on the boundary, and for any frequency, by simply summing over the contributions from each of the beams illuminating that observation point. This is the approach we adopt in this paper. We note that a similar approach was proposed in Groth (2011, Chapter 5), and for the 3D problem in Bi et al. (2011).
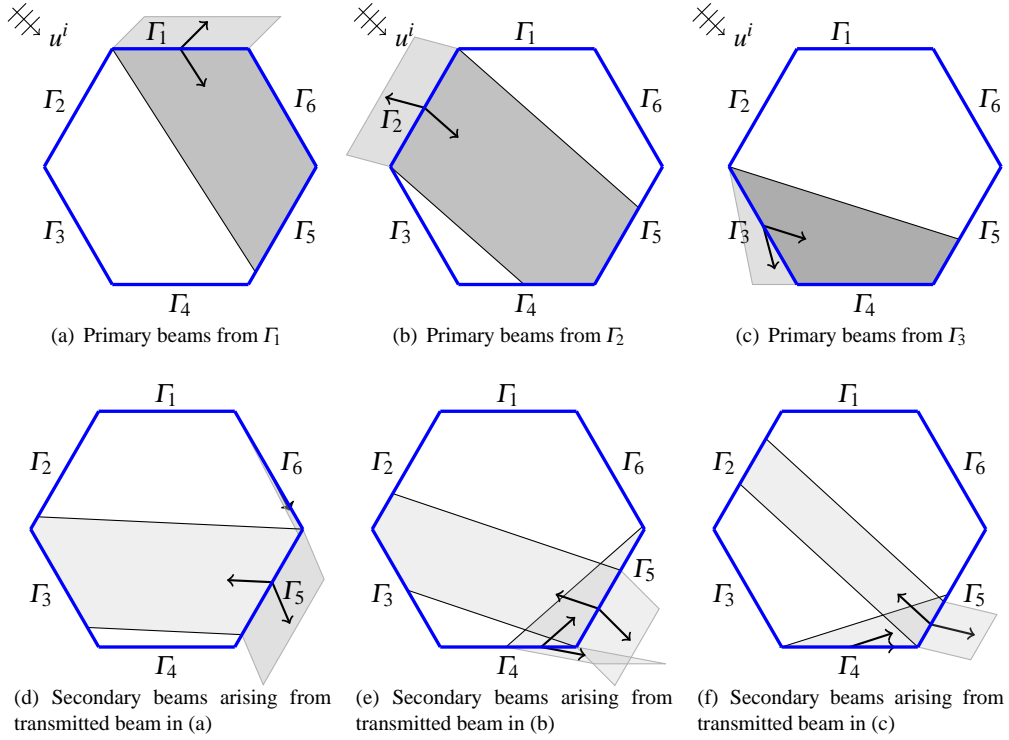

(a) Primary beams from Γ_1

(b) Primary beams from Γ_2

(c) Primary beams from Γ_3

(d) Secondary beams arising from transmitted beam in (a)

(e) Secondary beams arising from transmitted beam in (b)

(f) Secondary beams arising from transmitted beam in (c)

FIG. 2: Beam tracing in a hexagon. (a)-(c) show the primary reflected and transmitted beams arising from the incidence of u^i onto sides Γ_1-Γ_3 respectively. (d)-(f) show the secondary beams arising from the internal reflection and transmission to the exterior of the primary transmitted beams in (a)-(c) respectively. Note that in each of (d) and (f) the rays associated with one of the transmitted beams point along the side - this corresponds to total internal reflection (see §A.2.4).

As an illustration of the beam-tracing procedure, consider the configuration in Figure 2 where a penetrable hexagon is illuminated by a plane wave $u^i(\mathbf{x}) = e^{ik_1 \mathbf{d}^i \cdot \mathbf{x}}$ incident from the top left. In this case the incident wave strikes three of the sides of the hexagon, generating three beams of reflected rays, which propagate away to infinity, and three beams of transmitted waves, which propagate into the scatterer, as shown in Figure 2(a)–(c). Each of these transmitted beams has associated with it a plane wave of the form $ae^{ik_1(D\mathbf{d}+iE\mathbf{e})\cdot\mathbf{x}}$, where the amplitude a, the propagation and decay direction vectors $\mathbf{d} \in \mathbb{R}^2$ and $\mathbf{e} \in \mathbb{R}^2$, and the constants $D > 0$ and $E \geqslant 0$ are determined by the reflection/refraction laws presented in Appendix A. Each beam is bounded by a pair of limiting rays, which pass through the endpoints of the side of the polygon which generated the beam. Our algorithm takes these limiting rays to be parallel to the propagation direction $\mathbf{d}$, as illustrated in Figure 2 (but

see the discussion in Remark 3.1 below). The algorithm then tracks these limiting rays as they propagate across the interior of the scatterer, determines the points at which they re-intersect the boundary, and generates new transmitted and internally-reflected beams as appropriate, with associated plane wave directions and amplitudes again computed using the reflection/refraction laws in Appendix A. If the two re-intersection points of the limiting rays with the boundary lie on different sides of the polygon then multiple internally-reflected beams will be produced. Figure 2(d)–(f) shows the two such internally-reflected beams arising from the re-reflection of each of the three beams shown in Figure 2(a)–(c). The algorithm continues this process of internal re-reflection until a (user-specified) stopping criterion is achieved. In our experiments we stop tracking a beam when the amplitude of the next re-reflected wave divided by the amplitude of the original incident wave falls below machine precision. In our experiments this generally occurs after at most 50 orders of internal reflection (but often much sooner). We emphasise that the computational cost of the beam-tracing algorithm is completely independent of the wavenumber.

REMARK 3.1 For a beam with associated plane wave $a\mathrm{e}^{\mathrm{i}k_1(D\mathbf{d}+\mathrm{i}E\mathbf{e})\cdot\mathbf{x}}$, our algorithm takes the limiting rays bounding the beam to be parallel to the propagation direction $\mathbf{d}$. This is also the choice made in Bi et al. (2011), and it certainly seems a natural choice when the plane wave has no decay (i.e. when $E = 0$). But in the general case (in particular in an absorbing medium) it is not immediately obvious how to define the "ray direction", and hence where the "edges" of the beam should lie. What we are really asking, of course, is where the shadow boundaries between transmitted and diffracted waves lie in the related canonical diffraction problem of diffraction by an infinite absorbing transmission wedge (see §3.2.1 below). Given the lack of an exact (or even asymptotic) solution for this infinite wedge problem (as discussed in §1), we cannot currently make any further comment about this. But it is interesting to note that for the related (but simpler) problem of diffraction of a general plane wave in a homogeneous absorbing medium by a sound soft knife edge, for which an exact solution is available in terms of a Fresnel integral, the correct location of the shadow boundary (defined to be the *Stokes line* across which the incident field switches on/off) is *not* parallel to the real propagation vector of the plane wave beam. Rather, it is shifted somewhat in the direction of the imaginary propagation vector (Bertoni et al., 1978). It would be interesting to see whether an analogous adjustment in our beam-tracing algorithm improved the accuracy of the GO approximation, but we leave further investigation of this for future work.

3.2 *Approximating the diffracted component v_d*

We now consider the approximation of the diffracted component v_d by an HNA ansatz of the form (3.2). It is perhaps helpful to briefly review the approach taken in Hewett et al. (2012) for the analogous impenetrable problem of scattering by a sound soft convex polygon. In this case the HNA ansatz (1.1) (which involves only one wavenumber) contains just two terms in the summation, with phases $\psi^{\pm}(\mathbf{x}(s)) = \pm s$, where s is arc length measured anti-clockwise around the boundary. These correspond respectively to diffracted waves travelling anticlockwise and clockwise around the boundary. It is proved rigorously in Hewett et al. (2012) that this simple ansatz, when combined with piecewise polynomial approximation of the associated non-oscillatory amplitudes $v^{\pm}$, completely captures the oscillatory behaviour of the boundary solution. The remarkable success of the HNA methodology in this case is due to two factors. Firstly, the high frequency asymptotic behaviour of the solution to the canonical problem of diffraction by an infinite sound soft wedge is known - in fact there is an exact closed-form solution available (see, e.g., Bowman et al. (1969, §6.2)). This allows one to pick out the phases required to capture the primary diffracted waves. Secondly, the only multiple scattering effects in this case are the multiply-diffracted waves propagating around the boundary of the polygon. But each of these waves has one of the same two phases $\psi^{\pm}$ already included in the approximation space, so their contribution can be picked up in the amplitudes $v^{\pm}$.

By contrast (as discussed in §1), no exact (or even asymptotic) solution has yet been derived for the analogous canonical problem of diffraction by a penetrable wedge. Furthermore, for the penetrable case the multiply-scattered field is extremely complicated, featuring multiple reflections/refractions of the incident and diffracted fields, with potentially infinitely many different phases to consider in the approximation of v_d. Our approach in this paper is to first determine some qualitative information about the high frequency behaviour of the solution of the canonical wedge problem, and then to apply heuristic arguments, motivated by the basic principles of GTD for the impenetrable case, to design HNA approximation spaces incorporating just a small number of the

most important phases. For a detailed exposition of the GTD for the impenetrable case, we refer the reader to, e.g., Keller (1962), James (1986), or Borovikov & Kinber (1994).

3.2.1 Diffraction by a penetrable wedge

The canonical problem under consideration is the diffraction of a time-harmonic plane wave propagating in a medium of wavenumber k_1 by an infinite wedge of a second medium of wavenumber $k_2 \neq k_1$, with the total field and its normal derivative being continuous across the interface between the two media. For simplicity of exposition, we restrict attention to the case $k_1, k_2 > 0$, and in particular to the case $0 < k_1 < k_2$ (although the case $0 < k_2 < k_1$ can be dealt with similarly). Using the well-known correspondence (see, e.g., Borovikov & Kinber (1994, p. 351)) between the singularities of solutions of the time-dependent wave equation and the high frequency asymptotic behaviour of solutions of the Helmholtz equation, one can obtain qualitative information about the high frequency behaviour of the frequency domain wedge problem by considering the analogous time domain problem of diffraction of an incident plane pulse in a medium of wave speed c_1 by a wedge of wave speed c_2, with $0 < c_2 < c_1$. Here one can determine the position of the leading wavefronts associated with each of the components of the scattered field by appealing to Huygen's principle.
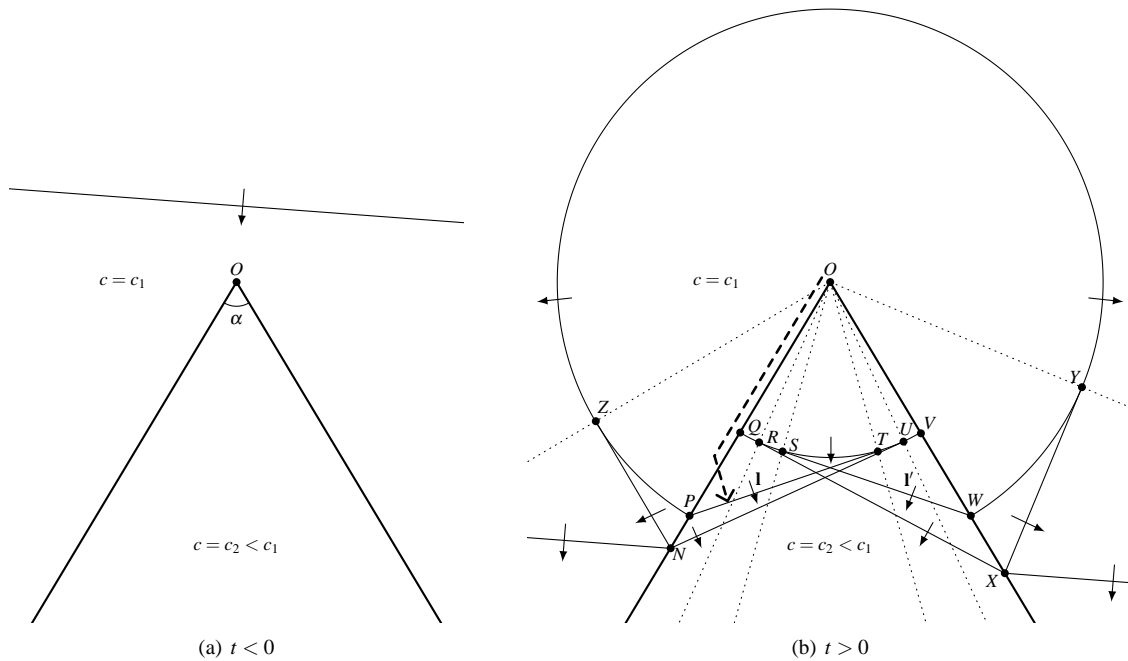

FIG. 3: Wavefront diagrams for time-domain diffraction by a penetrable wedge, in the case where $c_2 < c_1$ and $\alpha > \cos^{-1}(c_2/c_1)$. The incident wavefront is assumed not to be in contact with the wedge for $t < 0$ and to arrive at the point O at time $t = 0$. The dotted lines in (b) indicate shadow boundaries, and the thick dashed arrow represents a ray path associated with the lateral wavefront PT.

An illustration of the resulting wavefront diagrams for one particular scattering configuration is shown in Figure 3. Here we have assumed that the incident wavefront is not in contact with the wedge before it reaches the diffracting corner (see Figure 3(a)). After it reaches the corner, the wavefront structure shown in Figure 3(b) emerges. The incident wavefront now has two components (intersecting the wedge at N and X in Figure 3(b)), and there exist two planar reflected wavefronts (NZ and XY) and two planar transmitted wavefronts (NU and XR). The diffracted wavefronts in the exterior and interior are segments of the circles centered at O of radius c_1t ($PZYW$) and c_2t ($QRSTUV$) respectively (at time $t > 0$). In addition, Huygen's principle predicts the existence of so-called *lateral waves* (sometimes known as *head waves* or *bow waves*), with associated planar wavefronts (PT and WS). These waves can be associated with diffracted rays propagating along the exterior surface of the

wedge at speed c_1, which shed new rays propagating into the interior medium. A typical ray path is shown as a thick dashed arrow in Figure 3(b). Similar waves also appear in the scattering of the field due to a point source by a planar interface (cf. Brekhovskikh (1960, Chapter IV) and Jones (1964)). We note that Figure 3 shows only the simplest possible case, and more complicated wavefront configurations are possible. For example, for small enough wedge angles α the transmitted and lateral waves generated by one face of the wedge can be internally reflected by the other face, generating additional wavefronts. A sufficient and necessary condition for there to be no such internal reflection of the lateral waves is that $\alpha > \cos^{-1}(c_2/c_1)$.

In the original frequency domain wedge problem, we expect the structure of the field far from the corner to be analogous to that described above. That is, in the exterior we expect: an incident plane wave; two reflected plane wave beams, one bounded by the radial lines extending ON and OZ, and another bounded by the radial lines extending OX and OY; a diffracted wave with phase function $e^{ik_1 r}$, where r represents radial distance from the corner O. In the interior we expect: two transmitted plane wave beams; a diffracted wave with phase function $e^{ik_2 r}$; lateral waves with the phase functions $e^{ik_2 \mathbf{l} \cdot \mathbf{x}}$ and $e^{ik_2 \mathbf{l}' \cdot \mathbf{x}}$, where $\mathbf{l}, \mathbf{l}'$ are the direction vectors shown in Figure 3(b).

3.2.2 Approximation Space 1 - including diffraction from adjacent corners

We now use the qualitative analysis of the wedge diffraction problem presented in §3.2.1 to develop an HNA ansatz of the form (3.2) for the diffracted component v_d in the decomposition (3.1) of the solution to (2.8). In principle, in order to completely capture the oscillatory behaviour we would have to include phases corresponding to: (i) the diffracted and lateral waves emanating from each corner of the polygon, as described in §3.2.1; (ii) the (infinitely many) multiple internal re-reflections of these waves. However, in §4 we present convincing numerical evidence that an accurate and efficient approximation to v_d can be achieved with only a small number of carefully chosen phase functions. In fact we shall show results for two choices of approximation space for the numerical approximation of v_d. Both incorporate phases relating to the diffracted waves emanating from each of the corners of the polygon. Phases associated with the lateral waves and the multiple re-reflections of the diffracted and lateral waves are not included, but we give some ideas about how these could be included in future work in §3.2.4.

Our first approximation space (referred to as "Approximation Space 1" in §4) is defined as follows. On each side of the polygon we include phases corresponding to diffracted waves emanating from the corners adjacent to that side. That is, on each side of the polygon the phase functions in the approximation space are

$$\{e^{ik_1 s}, e^{-ik_1 s}, e^{ik_2 s}, e^{-ik_2 s}\}, \tag{3.3}$$

where s is arc length measured anticlockwise around the boundary. The phase functions (3.3) describe waves of both wavenumbers, propagating in both directions (clockwise and anticlockwise) around the boundary. This is the obvious generalisation of the approximation space used in Hewett et al. (2012) for the sound soft case, and leads to the following HNA ansatz for the total solution $v = (u, \partial u/\partial \mathbf{n})$:

$$v(\mathbf{x}) \approx v_{go}(\mathbf{x}) + v_1^+(\mathbf{x})e^{ik_1 s(\mathbf{x})} + v_1^-(\mathbf{x})e^{-ik_1 s(\mathbf{x})} + v_2^+(\mathbf{x})e^{ik_2 s(\mathbf{x})} + v_2^-(\mathbf{x})e^{-ik_2 s(\mathbf{x})}, \quad \mathbf{x} \in \Gamma. \tag{3.4}$$

Here v_1^+, v_2^+, v_1^-, v_2^- are amplitude functions which will be approximated by piecewise polynomials supported on overlapping graded meshes, designed to capture the expected singularities at the corners of the polygon. More precisely, on a typical side Γ_j of the polygon, v_1^+ and v_2^+ are approximated on a common geometric mesh graded towards the corner $\mathbf{P}_j$, and v_1^- and v_2^- are approximated on a common geometric mesh graded towards the corner $\mathbf{P}_{j+1}$, as illustrated in Figure 4.

To describe in more detail the meshes we use, we consider the case of a geometric mesh on the interval $[0, L]$, $L > 0$, refined towards 0. The meshes for approximating v_1^+, v_2^+, v_1^-, v_2^- on each side of the polygon are constructed from this basic building block by straightforward coordinate transformations. Given $n \geqslant 1$ (the number of layers in the mesh) we let $G_n(0, L)$ denote the set of meshpoints $\{x_i\}_{i=0}^n$ defined by

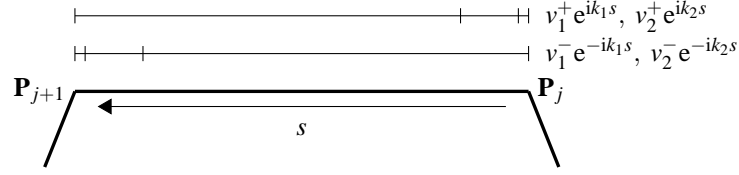$$x_0 := 0, \quad x_i := \sigma^{n-i} L, \quad i = 1, 2, \ldots, n,$$

FIG. 4: Illustration of overlapping geometrically graded meshes used to approximate the amplitudes v_1^+, v_2^+, v_1^-, v_2^- associated with the phase functions (3.3) on a typical side Γ_j.

where $0 < \sigma < 1$ is a grading parameter. A smaller grading parameter represents a more severe grading - in all of our experiments we take $\sigma = 0.15$, as in Hewett et al. (2012). Given a vector $\mathbf{p} \in (\mathbb{N}_0)^n$, we let $P_{\mathbf{p},n}(0,L)$ denote the space of piecewise polynomials on the mesh $G_n(0,L)$ with the degree vector $\mathbf{p}$, i.e.,

$$P_{\mathbf{p},n}(0,L) := \left\{ \rho : [0,L] \to \mathbb{C} : \rho|_{(x_{i-1},x_i)} \text{ is a polynomial of degree less than or equal to } (\mathbf{p})_i, i = 1,\ldots,n \right\}.$$

For reasons of efficiency and conditioning it is common to decrease the order of the approximating polynomials towards the singularity. Specifically, in all of our experiments we use a "linear slope" degree vector $\mathbf{p}$ with

$$(\mathbf{p})_i := \begin{cases} p - \left\lfloor \frac{(n+1-i)}{n}p \right\rfloor, & 1 \leqslant i \leqslant n-1, \\ p, & i = n, \end{cases}$$

where the integer $p \geqslant 0$ is the highest polynomial degree on the mesh.

For simplicity we assume the same number of layers, n, in each of the graded meshes on the polygon. We adopt an "hp" refinement approach (as in Hewett et al. (2012)) in which the number of degrees of freedom is increased by increasing the polynomial degree p, while simultaneously refining the meshes. Specifically, in all our experiments we take $n = p+1$. On each graded mesh we have at most $(p/2n)(n^2-n+2)+2n-1 = (p^2 + 3p)/2$ degrees of freedom defining the piecewise polynomials. Since we have four amplitudes to approximate on each side, each of which has an associated graded mesh, the total number of degrees of freedom in the approximation space is at most $2n_s(p^2+3p)$.

3.2.3 Approximation Space 2 - including also diffraction from non-adjacent corners

Our second approximation space (referred to as "Approximation Space 2" in §4) is constructed by supplementing Approximation Space 1 with the phases corresponding to diffracted waves emanating from non-adjacent corners. That is, on a given side Γ_j of the polygon the phase functions in the approximation space are

$$\{e^{ik_1 s}, e^{-ik_1 s}, e^{ik_2 s}, e^{-ik_2 s}, e^{ik_2 r_1}, \ldots, e^{ik_2 r_{n_s-2}}\}, \tag{3.5}$$

where r_i, $i = 1,\ldots,n_s - 2$ are the radial distances from the corners non-adjacent to the side in question (there are $n_s - 2$ such corners since the polygon is convex), and the ansatz (3.4) is supplemented by a sum

$$w_1(\mathbf{x})e^{ik_2 r_1(\mathbf{x})} + \ldots + w_{n_s-2}(\mathbf{x})e^{ik_2 r_{n_s-2}(\mathbf{x})}, \quad \mathbf{x} \in \Gamma, \tag{3.6}$$

where the amplitudes w_i, $i = 1,\ldots,n_s - 2$, are approximated numerically by piecewise polynomials.

We expect the amplitudes w_i to have a (possibly infinite) number of discontinuities, to compensate for the discontinuities inherent in the GO approximation (where we cut off the plane wave beams sharply across the beam boundaries). In principle one should therefore approximate each w_i on a mesh refined towards each of these discontinuities. However, for simplicity we take into account only those discontinuities arising from the lowest order GO terms, i.e. the primary transmitted waves. In the configuration illustrated in Figure 3(b) the discontinuities in question are across the shadow boundaries (indicated by the dotted lines) extending *OR* and *OU*.

To approximate an amplitude w_i we therefore proceed as follows. We start with a single element living on the whole side Γ_j. Then if (during the beam-tracing algorithm for computing the GO term) the corner associated

with the radial distance r_i produced any beam boundaries associated with primary transmitted beams, we check whether these beam boundaries intersect the side Γ_j. If they do, we put new mesh points at the intersection points; see Figure 5 for an illustration of this procedure. Since there are at most two such beam boundaries, the side Γ_j gets subdivided into at most three elements. On each of these resulting elements we approximate w_i by a single polynomial of degree p, where p is the same as for the Approximation Space 1 amplitudes. Carrying out this procedure for each $i = 1, \ldots, n_s - 2$ adds at most $3(n_s - 2)(p + 1)$ degrees of freedom on the side Γ_j; extending the same procedure to all the other sides results in at most $3n_s(n_s - 2)(p + 1)$ degrees of freedom being added in total when we go from Approximation Space 1 to Approximation Space 2.
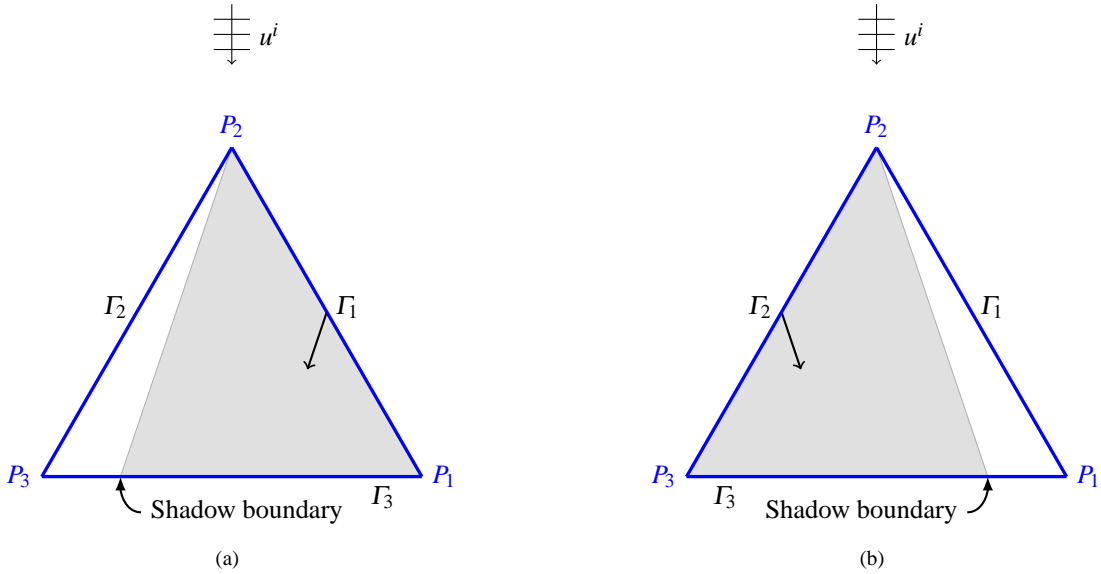

FIG. 5: Shadow boundaries in an equilateral triangle. Determining the mesh on Γ_3 associated with the approximation of the amplitude of the diffracted term arising from the non-adjacent corner P_2. Mesh points are introduced at the locations of the shadow boundaries associated with the primary transmitted waves from sides Γ_1 and Γ_2, as illustrated in (a) and (b) respectively. The resulting mesh on Γ_3 has three elements.

3.2.4 Including other phase functions

We expect that even more accurate approximations could be obtained by including the effects of higher order terms in the asymptotic approximation. Firstly, one could include phases associated with the lateral waves associated with each corner of the polygon. Secondly, one could include phases associated with the (multiple) internal reflection of (i) the diffracted waves and (ii) the lateral waves. The phases for (i) could be computed using an image method (i.e. introducing "image corners" in a non-physical image domain outside the scatterer). The phases for (ii) could be determined using a simple modification of the beam-tracing algorithm described in §3.1. We do not consider these generalisations any further here.

4 Numerical examples

In the previous section, two approximation spaces ("Approximation Space 1", defined in §3.2.2, and "Approximation Space 2", defined in §3.2.3) were proposed for the approximation of v_d (note that we use the same approximation space for each component of v_d). In this section we demonstrate via various numerical examples that using these to approximate v with just a small number of degrees of freedom, either via the ansatz (3.4), or else supplementing that further with (3.6), provides a significant improvement over GO. More precisely, our results below demonstrate that, for all absorptions and wavenumbers tested, the best fit from Approximation

Space 2 to both u and $\partial u/\partial \mathbf{n}$ on Γ is at least 50% more accurate (and in many cases much better than this) than the approximation achieved using GO alone, using fewer than 200 degrees of freedom. We show further (in Table 2 below) that for a fixed number of degrees of freedom the relative error in our best approximation from Approximation Space 2 to both u_d and $\partial u_d/\partial \mathbf{n}$ does not grow significantly as frequency increases.

For each example considered below, we first obtain a reference solution $v_{\mathrm{ref}} \approx v$ by solving (2.8) using a conventional hp-BEM with a sufficient number of degrees of freedom to ensure that the relative error

$$\|v - v_{\mathrm{ref}}\|_{L^2(\Gamma)}/\|v\|_{L^2(\Gamma)}$$

is of the order of 10^{-4}. Henceforth, for ease of presentation we shall denote this reference solution v_{ref} simply as v. Next, we compute an approximation to v_{go}, following the procedure described in §3.1. Finally, a least squares approach is employed to find the best fit from each of Approximation Spaces 1 and 2 to $v_d = v - v_{go}$ in the L^2 norm. This is carried out by discretising the L^2 norm to be minimised using a large number of equally spaced quadrature points on each side, and solving the resulting discrete least squares problem. We denote the approximation to v achieved via this procedure using Approximation Space j by $V_j = (U_j, W_j)$, $j = 1, 2$.

Throughout this section, we consider scattering by an equilateral triangle with side length 2π. We consider four different incident angles, as shown in Figure 6, and we consider four different levels of absorption, governed by the imaginary part of the refractive index. Specifically, the real part of the refractive index is taken to be 1.31 throughout, which is approximately that of ice, the scattering properties of which are of great interest in aspects of meteorology and physics (see, e.g., Baran (2012)), as mentioned in §1 (note though that the techniques presented are applicable to convex polygons of any shape and any refractive index). So, for any given exterior wavenumber k_1, the interior wavenumber is $k_2 = k_1(1.31 + \xi i)$, with the value of ξ determining the level of absorption . The total field (computed using our reference solution) for angle 4, $k_1 = 10$, and for $\xi = 0$ (no absorption) and $\xi = 0.05$ is shown in Figure 1.
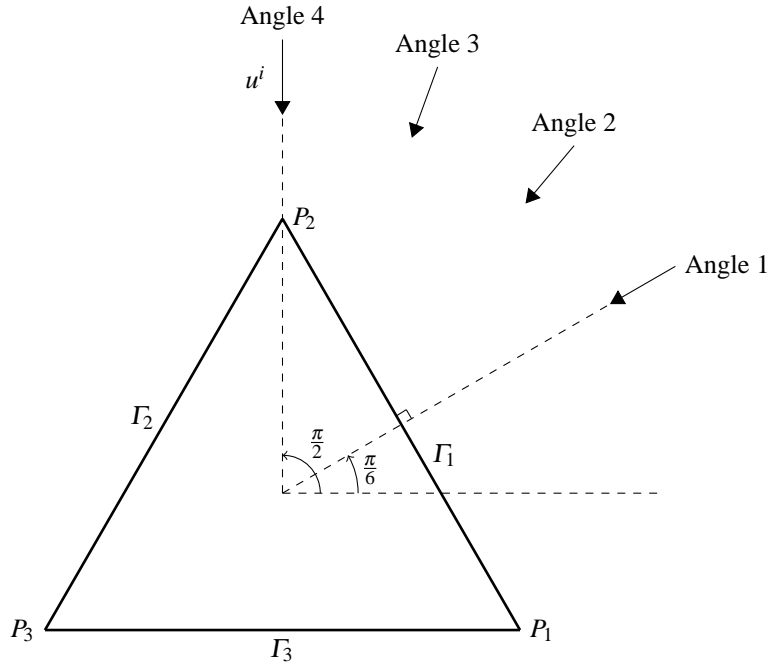
FIG. 6: Incident directions used in numerical experiments (angles 1–4 are equally spaced).

In Figure 7(a) we plot the real part of $u_d = u - u_{go}$ (computed from the reference solution), $U_1 - u_{go}$ and $U_2 - u_{go}$ (the approximations to u_d using Approximation Spaces 1 and 2 respectively), for $k_1 = 20$, $\xi = 0.025$, and incident angle 4. On the two sides that are illuminated by the incident wave (Γ_1 and Γ_2), the best fit is fairly

accurate for each approximation space. However, on Γ_3, the side in shadow, Approximation Space 2 provides a much better fit. This is not surprising, since this space also includes the effect on Γ_3 of the diffracted wave from P_2, which, for this incident direction, is relatively stronger than the effects on Γ_1 and Γ_2 of the diffracted waves from P_3 and P_1 respectively. Figure 7(b) shows the differences $u - U_1$ and $u - U_2$, to better illustrate the quality of the two fits.
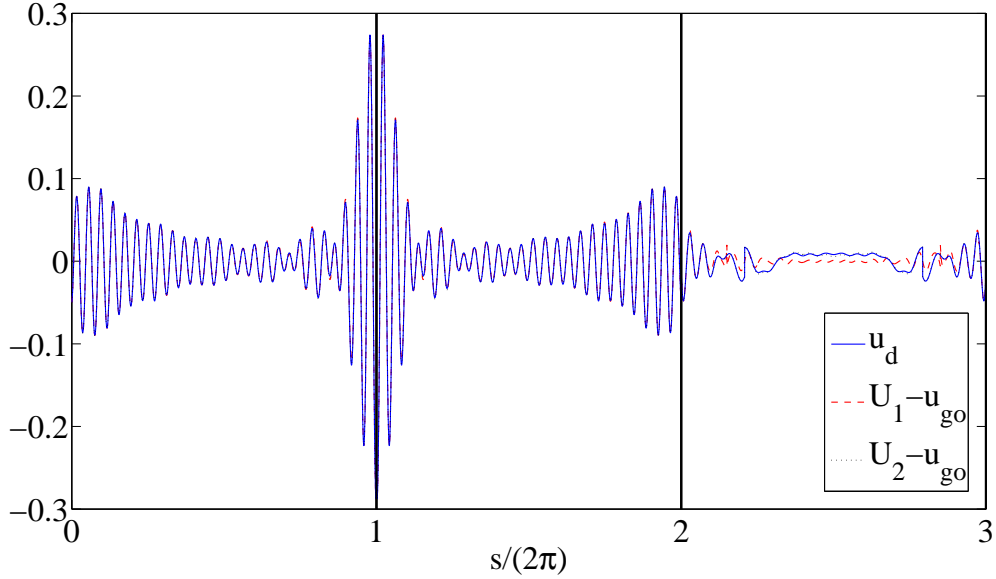
(a) Real part of u_d, $U_1 - u_{go}$ and $U_2 - u_{go}$ on the boundary.
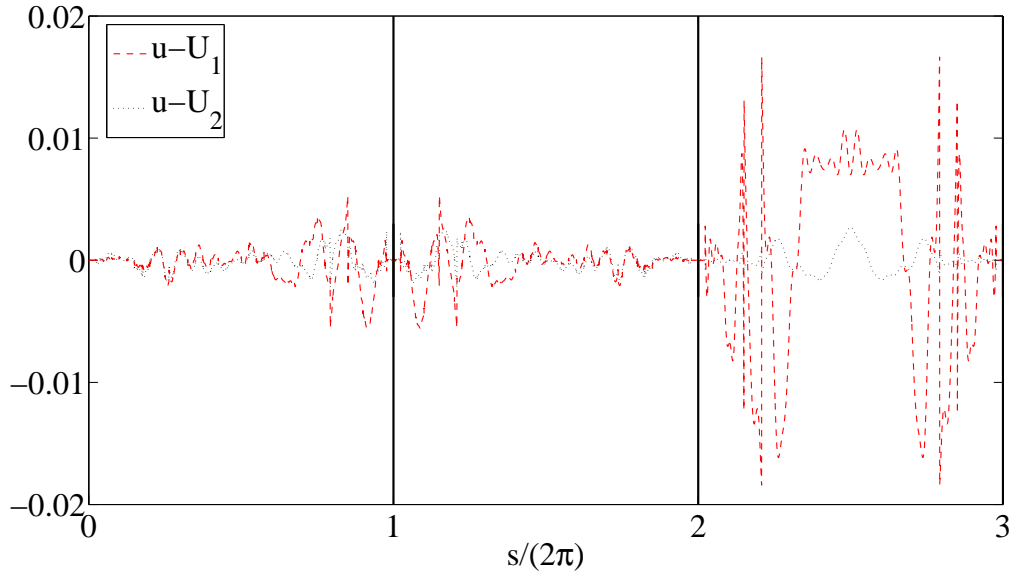
(b) Real part of the difference between the reference solution and the best approximations U_1 and U_2.

FIG. 7: Scattering by the triangle in Figure 6 with $k_1 = 20$, $\xi = 0.025$, and incident angle 4. Here s represents arc length measured anti-clockwise from P_1.

In Figure 8, we show the accuracy of the approximation to u using GO and each approximation space, for

a range of values of k_1, for $\xi = 0.05$, and for angles 1, 2, 3 and 4. Here and throughout this section we take $p = 4$ for both Approximation Spaces 1 and 2, as detailed in §3.2.2 and §3.2.3, giving a total number of degrees of freedom of 168 for Approximation Space 1, and 193 for Approximation Space 2. All norms in Figure 8 (and in Tables 1 and 2) are approximations to $\| \cdot \|_{L^2(\Gamma)}$ computed using a large number of evaluation points. For small values of k_1, Approximation Space 2 provides a noticeably better fit than Approximation Space 1, and in each case both approximation spaces achieve a significant improvement over GO for all values of k_1, with the error in the approximation using Approximation Space 1 being less than half that of GO alone, and the approximation obtained using Approximation Space 2 being better still. As k_1 increases, the difference between Approximation Spaces 1 and 2 becomes less noticeable, reflecting the faster decay of diffracted waves propagating within the scatterer at higher frequencies. For angles 3 and 4, and for larger values of k_1, the errors in our approximation are close to the accuracy of our reference solution, indicating that, in these cases, we are capturing the oscillatory behaviour of the diffracted field extremely well using the phase functions (3.5).
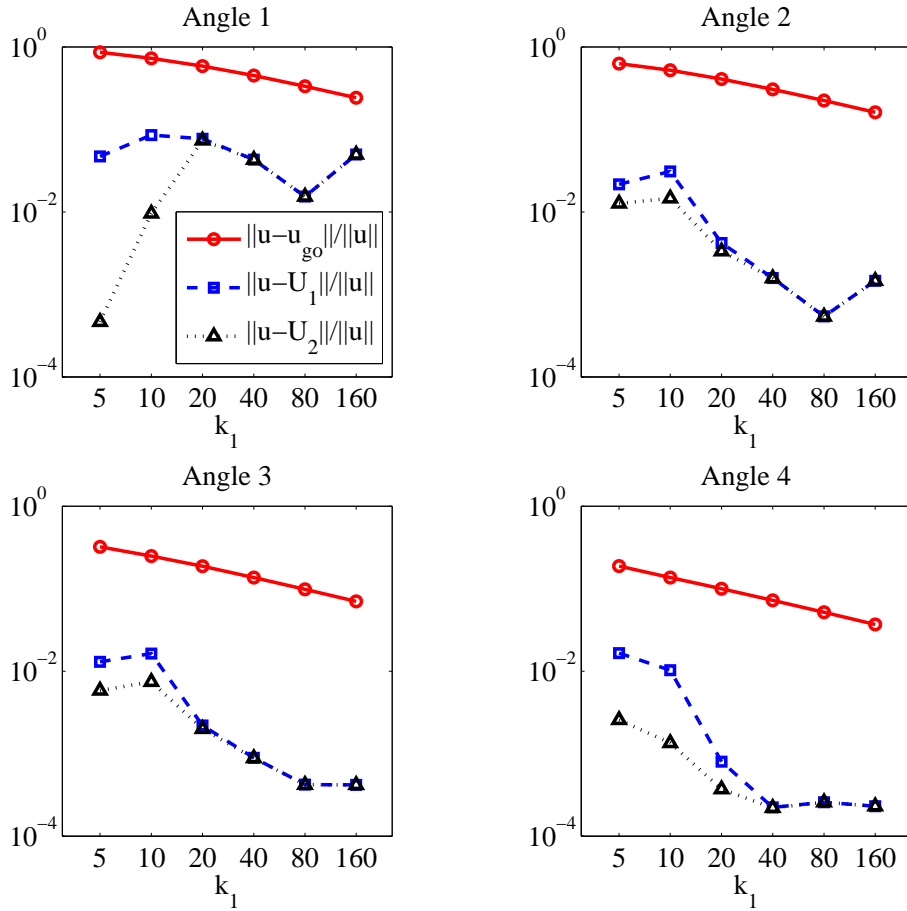
FIG. 8: Relative errors in approximations for fixed absorption $\xi = 0.05\mathrm{i}$, varying incident angle.

Next, in Table 1 we consider varying absorption for incident angle 4 and for a range of k_1. For $\xi \geqslant 0.0125$, the relative errors achieved by Approximation Space 2 are less than 1% for all values of k_1 tested, and Approximation Space 1 performs only slightly worse, particularly for larger k_1. Even for zero absorption, the error achieved with Approximation Space 2 is of the order of 2%–3%, whilst the error with GO alone is of the order of 10% even for reasonably large k_1. As the absorption ξ decreases, the importance of including the extra diffraction term in Approximation Space 2 becomes apparent. These results are very promising, in that they show that

k_1	ξ	$\dfrac{\lVert u-u_{go}\rVert}{\lVert u\rVert}$	$\dfrac{\lVert u-U_1\rVert}{\lVert u\rVert}$	$\dfrac{\lVert u-U_2\rVert}{\lVert u\rVert}$	$\dfrac{\lVert \frac{\partial u}{\partial \mathbf{n}}-(\frac{\partial u}{\partial \mathbf{n}})_{go}\rVert}{\lVert \frac{\partial u}{\partial \mathbf{n}}\rVert}$	$\dfrac{\lVert \frac{\partial u}{\partial \mathbf{n}}-W_1\rVert}{\lVert \frac{\partial u}{\partial \mathbf{n}}\rVert}$	$\dfrac{\lVert \frac{\partial u}{\partial \mathbf{n}}-W_2\rVert}{\lVert \frac{\partial u}{\partial \mathbf{n}}\rVert}$
5	0.05	1.88×10^{-1}	1.66×10^{-2}	2.57×10^{-3}	1.56×10^{-1}	1.62×10^{-2}	1.97×10^{-3}
10	0.05	1.37×10^{-1}	1.03×10^{-2}	1.35×10^{-3}	7.76×10^{-2}	1.03×10^{-2}	1.26×10^{-3}
20	0.05	1.00×10^{-1}	8.41×10^{-4}	3.72×10^{-4}	5.60×10^{-2}	1.53×10^{-3}	1.35×10^{-3}
40	0.05	7.25×10^{-2}	2.23×10^{-4}	2.20×10^{-4}	4.04×10^{-2}	1.04×10^{-3}	1.04×10^{-3}
80	0.05	5.19×10^{-2}	2.58×10^{-4}	2.58×10^{-4}	2.88×10^{-2}	7.69×10^{-4}	7.69×10^{-4}
160	0.05	3.69×10^{-2}	2.31×10^{-4}	2.31×10^{-4}	2.05×10^{-2}	6.49×10^{-4}	6.49×10^{-4}
5	0.025	2.19×10^{-1}	3.03×10^{-2}	5.53×10^{-3}	1.55×10^{-1}	2.94×10^{-2}	4.14×10^{-3}
10	0.025	1.54×10^{-1}	4.09×10^{-2}	4.49×10^{-3}	9.87×10^{-2}	4.41×10^{-2}	3.73×10^{-3}
20	0.025	1.10×10^{-1}	1.15×10^{-2}	2.00×10^{-3}	6.35×10^{-2}	1.12×10^{-2}	2.22×10^{-3}
40	0.025	8.09×10^{-2}	7.01×10^{-4}	3.37×10^{-4}	4.58×10^{-2}	1.19×10^{-3}	1.04×10^{-3}
80	0.025	5.85×10^{-2}	3.42×10^{-4}	3.41×10^{-4}	3.30×10^{-2}	7.69×10^{-4}	7.69×10^{-4}
160	0.025	4.19×10^{-2}	2.80×10^{-4}	2.80×10^{-4}	2.35×10^{-2}	6.44×10^{-4}	6.44×10^{-4}
5	0.0125	2.48×10^{-1}	4.05×10^{-2}	8.02×10^{-3}	1.90×10^{-1}	3.94×10^{-2}	5.96×10^{-3}
10	0.0125	1.84×10^{-1}	7.88×10^{-2}	9.46×10^{-3}	1.35×10^{-1}	8.07×10^{-2}	7.69×10^{-3}
20	0.0125	1.28×10^{-1}	4.53×10^{-2}	9.42×10^{-3}	8.05×10^{-2}	4.41×10^{-2}	8.49×10^{-3}
40	0.0125	9.13×10^{-2}	1.05×10^{-2}	2.66×10^{-3}	5.03×10^{-2}	1.01×10^{-2}	2.56×10^{-3}
80	0.0125	6.69×10^{-2}	1.87×10^{-3}	1.79×10^{-3}	3.61×10^{-2}	1.04×10^{-3}	9.07×10^{-4}
160	0.0125	4.84×10^{-2}	7.52×10^{-4}	7.52×10^{-4}	2.60×10^{-2}	6.68×10^{-4}	6.68×10^{-4}
5	0	2.57×10^{-1}	5.30×10^{-2}	1.16×10^{-2}	2.30×10^{-1}	5.17×10^{-2}	8.57×10^{-3}
10	0	2.15×10^{-1}	1.43×10^{-1}	1.95×10^{-2}	1.99×10^{-1}	1.49×10^{-1}	1.60×10^{-2}
20	0	1.79×10^{-1}	1.48×10^{-1}	2.82×10^{-2}	1.65×10^{-1}	1.47×10^{-1}	2.25×10^{-2}
40	0	1.50×10^{-1}	1.34×10^{-1}	3.07×10^{-2}	1.39×10^{-1}	1.31×10^{-1}	2.37×10^{-2}
80	0	1.25×10^{-1}	1.17×10^{-1}	3.17×10^{-2}	1.17×10^{-1}	1.13×10^{-1}	2.30×10^{-2}
160	0	1.04×10^{-1}	1.00×10^{-1}	2.81×10^{-2}	9.80×10^{-2}	9.58×10^{-2}	2.07×10^{-2}

Table 1: Relative errors in approximation of u and $\partial u/\partial \mathbf{n}$, using GO and each approximation space, for a range of values of k_1, for incident angle 4 and for varying absorption ξ.

by including the phases associated with the "leading order" diffracted waves in our approximation space (i.e. Approximation Space 2), we can obtain an accuracy that is suitable for many applications. By including further phase functions corresponding to higher order internal reflections of these diffracted waves and also the lateral waves (as mentioned in §3.2.4) we conjecture that it might be possible to achieve even higher accuracy in our approximation, although of course that would be at the expense of requiring more degrees of freedom.

In order to compare the relative accuracy of our best approximations from Approximation Spaces 1 and 2 to the diffracted component v_d as k_1 increases, in Table 2 we show the approximation errors relative to u_d and $\partial u_d/\partial \mathbf{n}$ for incident angle 4 and for the four values of ξ. These results demonstrate that for a fixed number of degrees of freedom the relative error in our best approximation from Approximation Space 2 does not grow significantly as frequency increases. The same is also true for Approximation Space 1 for $\xi \geqslant 0.0125$, but when $\xi = 0$ Approximation Space 1 does not give good results at higher frequencies, highlighting the need to include the effect of diffraction from non-adjacent corners (as is included in Approximation Space 2) in this case. This suggests that the phase functions in the two approximation spaces are correctly capturing the most significant oscillations of the diffracted component of the scattered field.

Finally we look at how the accuracy of our approximations to the solution on the boundary affects the approximation of the far field pattern. For many applications, such as light scattering by atmospheric particles, it may be the scattering pattern far from the scatterer that is really of primary interest. In the 2D case, an asymptotic expansion of the representation (2.6), taking into account the asymptotic behaviour of the Hankel functions for large argument (see, e.g., Olver et al. (2010)), gives the expression for the scattered field $u^s := u_1 - u^i$ far from

k_1	ξ	$\dfrac{\lVert u-U_1 \rVert}{\lVert u_d \rVert}$	$\dfrac{\lVert u-U_2 \rVert}{\lVert u_d \rVert}$	$\dfrac{\lVert \frac{\partial u}{\partial \mathbf{n}}-W_1 \rVert}{\lVert \frac{\partial u_d}{\partial \mathbf{n}} \rVert}$	$\dfrac{\lVert \frac{\partial u}{\partial \mathbf{n}}-W_2 \rVert}{\lVert \frac{\partial u_d}{\partial \mathbf{n}} \rVert}$
5	0.05	8.85×10^{-2}	1.37×10^{-2}	1.41×10^{-1}	1.71×10^{-2}
10	0.05	7.52×10^{-2}	9.88×10^{-3}	1.32×10^{-1}	1.62×10^{-2}
20	0.05	8.40×10^{-3}	3.71×10^{-3}	2.73×10^{-2}	2.41×10^{-2}
40	0.05	3.08×10^{-3}	3.04×10^{-3}	2.56×10^{-2}	2.56×10^{-2}
80	0.05	4.98×10^{-3}	4.97×10^{-3}	2.67×10^{-2}	2.67×10^{-2}
160	0.05	6.24×10^{-3}	6.24×10^{-3}	3.16×10^{-2}	3.16×10^{-2}
5	0.025	1.39×10^{-1}	2.53×10^{-2}	1.90×10^{-1}	2.67×10^{-2}
10	0.025	2.65×10^{-1}	2.91×10^{-2}	4.20×10^{-1}	3.78×10^{-2}
20	0.025	1.04×10^{-1}	1.81×10^{-2}	1.76×10^{-1}	3.50×10^{-2}
40	0.025	8.66×10^{-3}	4.16×10^{-3}	2.60×10^{-2}	2.26×10^{-2}
80	0.025	5.84×10^{-3}	5.83×10^{-3}	2.33×10^{-2}	2.33×10^{-2}
160	0.025	6.69×10^{-3}	6.69×10^{-3}	2.73×10^{-2}	2.73×10^{-2}
5	0.0125	1.65×10^{-1}	3.24×10^{-2}	2.10×10^{-1}	3.14×10^{-2}
10	0.0125	4.28×10^{-1}	5.14×10^{-2}	6.00×10^{-1}	5.72×10^{-2}
20	0.0125	3.54×10^{-1}	6.27×10^{-2}	5.48×10^{-1}	8.78×10^{-2}
40	0.0125	1.15×10^{-1}	3.25×10^{-2}	2.01×10^{-1}	5.65×10^{-2}
80	0.0125	2.79×10^{-2}	2.68×10^{-2}	2.87×10^{-2}	2.52×10^{-2}
160	0.0125	1.55×10^{-2}	1.55×10^{-2}	2.57×10^{-2}	2.57×10^{-2}
5	0	2.06×10^{-1}	4.51×10^{-2}	2.25×10^{-1}	3.72×10^{-2}
10	0	6.55×10^{-1}	9.09×10^{-2}	7.49×10^{-1}	8.07×10^{-2}
20	0	8.26×10^{-1}	1.58×10^{-1}	8.91×10^{-1}	1.37×10^{-1}
40	0	8.98×10^{-1}	2.05×10^{-1}	9.45×10^{-1}	1.71×10^{-1}
80	0	9.38×10^{-1}	2.53×10^{-1}	9.67×10^{-1}	1.97×10^{-1}
160	0	9.59×10^{-1}	2.52×10^{-1}	9.78×10^{-1}	1.89×10^{-1}

Table 2: Relative errors in approximation of u_d and $\partial u_d / \partial \mathbf{n}$, using each approximation space, for a range of values of k_1, for incident angle 4 and for varying absorption ξ.

the scatterer as

$$u^s(\mathbf{x}) \sim \frac{\mathrm{e}^{\mathrm{i}\pi/4}}{2\sqrt{2\pi}} \frac{\mathrm{e}^{\mathrm{i}kr}}{\sqrt{kr}} F(\hat{\mathbf{x}}), \quad \text{as } r := |\mathbf{x}| \to \infty,$$

where $\hat{\mathbf{x}} := \mathbf{x}/|\mathbf{x}| \in \mathbb{S}^1$, the unit circle, and the far field pattern F is given by

$$F(\hat{\mathbf{x}}) = -\int_\Gamma \mathrm{e}^{-\mathrm{i}k\hat{\mathbf{x}} \cdot \mathbf{y}} \left(\mathrm{i}k(\hat{\mathbf{x}} \cdot n(\mathbf{y}))u(\mathbf{y}) + \frac{\partial u}{\partial \mathbf{n}}(\mathbf{y}) \right) \mathrm{d}s(\mathbf{y}), \quad \hat{\mathbf{x}} \in \mathbb{S}^1. \tag{4.1}$$

We plot the far field pattern $F(\hat{\mathbf{x}}(t))$, $t \in [0, 2\pi]$ for incident angle 4, absorption $\xi = 0.05$ and for $k_1 = 5$ and $k_1 = 160$ in Figure 9, where $t = 0$ corresponds to the direction from which u^i is incident, $\hat{\mathbf{x}}(t)$ is a point at angular distance t round the unit circle, and we have computed F by inserting our reference solutions u and $\partial u / \partial \mathbf{n}$ into (4.1).

In Table 3 we compare the value of F computed using the reference solutions with that computed using GO (F_{go}), Approximation Space 1 (F_1) and Approximation Space 2 (F_2). Here, the norms represent approximations to $\| \cdot \|_{L^2(\mathbb{S}^1)}$ computed using a large number of evaluation points. Even for the worst incident angle, namely angle 1, we still obtain approximations that are within roughly 1% of the reference far field pattern using Approximation Space 2 (and in most cases the same is true for Approximation Space 1), representing a significant improvement over GO, particularly for lower values of k_1. For the other angles, the results are even better (note that the tailing off of the error as k_1 gets large may be due to the fact that our reference solution is only accurate to order 10^{-4}). As mentioned in §1, the approach of mapping the GO solution on the boundary to the far-field using an integral equation representation is sometimes called the physical-geometric optics hybrid
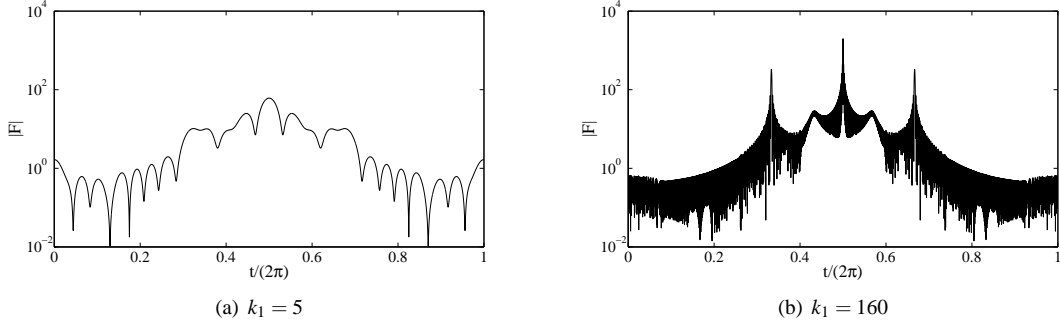
FIG. 9: Far-field pattern, $|F(\hat{\mathbf{x}}(t))|$, for $k_1 = 5$ and $k_1 = 160$, $\xi = 0.05$, incident angle 4.

method (see Bi et al. (2011)). Our results demonstrate that it is possible to achieve a significant improvement on this approach using a small amount of additional computation.

k_1	Angle	$\frac{\|F-F_{go}\|}{\|F\|}$	$\frac{\|F-F_1\|}{\|F\|}$	$\frac{\|F-F_2\|}{\|F\|}$
5	1	5.92×10^{-1}	1.67×10^{-2}	2.43×10^{-5}
10	1	2.38×10^{-1}	1.00×10^{-1}	7.02×10^{-3}
20	1	1.30×10^{-1}	2.71×10^{-2}	2.78×10^{-2}
40	1	9.02×10^{-2}	1.09×10^{-2}	1.09×10^{-2}
80	1	6.33×10^{-2}	7.14×10^{-3}	7.14×10^{-3}
160	1	4.46×10^{-2}	1.23×10^{-2}	1.23×10^{-2}
5	2	1.90×10^{-1}	7.52×10^{-3}	7.01×10^{-5}
10	2	2.04×10^{-1}	3.29×10^{-2}	6.21×10^{-3}
20	2	1.26×10^{-1}	3.90×10^{-3}	2.33×10^{-3}
40	2	9.07×10^{-2}	1.18×10^{-3}	1.17×10^{-3}
80	2	6.44×10^{-2}	3.87×10^{-4}	3.83×10^{-4}
160	2	4.56×10^{-2}	4.77×10^{-4}	4.77×10^{-4}
5	3	9.44×10^{-2}	7.88×10^{-3}	5.41×10^{-3}
10	3	9.65×10^{-2}	1.44×10^{-2}	6.40×10^{-3}
20	3	6.54×10^{-2}	1.90×10^{-3}	1.69×10^{-3}
40	3	4.75×10^{-2}	7.14×10^{-4}	7.13×10^{-4}
80	3	3.41×10^{-2}	2.46×10^{-4}	2.44×10^{-4}
160	3	2.42×10^{-2}	2.26×10^{-4}	2.26×10^{-4}
5	4	5.93×10^{-2}	2.72×10^{-3}	4.52×10^{-5}
10	4	3.67×10^{-2}	8.98×10^{-3}	9.08×10^{-4}
20	4	2.54×10^{-2}	7.16×10^{-4}	2.74×10^{-4}
40	4	1.85×10^{-2}	1.17×10^{-4}	1.14×10^{-4}
80	4	1.31×10^{-2}	1.04×10^{-4}	1.04×10^{-4}
160	4	9.35×10^{-3}	1.04×10^{-4}	1.04×10^{-4}

Table 3: Far-field errors for various k_1, with absorption $\xi = 0.05$, various incident angles.

In summary, our numerical examples demonstrate that HNA approximation spaces of the form (3.2) can provide efficient approximations for problems of scattering by penetrable scatterers. The two specific approximation spaces we considered are perhaps the simplest extensions to the penetrable case of the spaces used for impenetrable scatterers (see Chandler-Wilde et al. (2012a)). Regardless, we have shown that they provide an accuracy sufficient for many applications, across a range of absorptions and frequencies, significantly outperforming GO in each case with only a small number of degrees of freedom, fixed independently of the

wavenumber. We anticipate that the addition of further phase functions corresponding to lateral waves and the reflections of diffracted waves would allow for higher accuracy to be achieved, although at the expense of a higher complexity in the algorithm and slightly higher computational cost. The justification of this claim is left to future work.

A Reflection/refraction at a planar interface

In this appendix we present a full derivation of the laws of reflection and refraction at a planar interface between two propagation media of arbitrary absorption.

A.1 *Plane wave propagation in an absorbing medium*

We consider time-harmonic scalar waves modelled by the Helmholtz equation

$$\Delta u + k^2 u = 0, \tag{A.1}$$

with a complex wavenumber k. We shall write

$$k = k_0(\mu + i\xi),$$

where $k_0 > 0$ is a reference real wavenumber, and $\mu + i\xi$ is the refractive index of the medium. We shall assume throughout that $\mu > 0$ and $\xi \geqslant 0$; the case $\xi = 0$ corresponds to a non-absorbing medium, and the case $\xi > 0$ corresponds to an absorbing medium. We consider solutions of (A.1) of the form

$$u(\mathbf{x}) = A e^{i k_0 \mathbf{V} \cdot \mathbf{x}}, \qquad \mathbf{x} \in \mathbb{R}^2, \tag{A.2}$$

which represents a plane wave with complex amplitude A and complex propagation vector $\mathbf{V}$. It is convenient to split $\mathbf{V}$ into real and imaginary components, writing

$$\mathbf{V} = D\mathbf{d} + iE\mathbf{e},$$

where $\mathbf{d}$ and $\mathbf{e}$ are real unit vectors and D, E are real scalars, after which (A.2) becomes

$$u(\mathbf{x}) = A \exp\{i k_0 (D\mathbf{d} + iE\mathbf{e}) \cdot \mathbf{x}\}. \tag{A.3}$$

Note that the vectors $\mathbf{d}$ and $\mathbf{e}$ are normal to the planes of constant phase and constant amplitude of u, respectively. Without loss of generality we may assume that $\mathbf{d} \cdot \mathbf{e} \geqslant 0$. If $\mathbf{d} = \mathbf{e}$, then the wave is called *homogeneous*, otherwise it is *inhomogeneous*. In order to find the relationship between $\mathbf{d}, \mathbf{e}, D, E$ and the components μ, ξ of the refractive index, we substitute (A.3) into the Helmholtz equation (A.1), which, after equating the real and imaginary parts, gives

$$D^2 - E^2 \;\; = \;\; \mu^2 - \xi^2, \tag{A.4}$$
$$(D\mathbf{d}) \cdot (E\mathbf{e}) \;\; = \;\; \mu\xi. \tag{A.5}$$

We note from (A.4)–(A.5) that we cannot have $D = 0$; otherwise (A.5) would imply that $\xi = 0$ (since $\mu > 0$ by assumption), and (A.4) would then give the contradiction $-E^2 = \mu^2$. Without loss of generality we may assume that $D > 0$ (we can multiply both $\mathbf{d}$ and $\mathbf{e}$ by minus one if necessary). Now, if $\xi > 0$ then $\mu\xi > 0$ and (A.5) implies that $\mathbf{d} \cdot \mathbf{e} > 0$ and $DE > 0$, so that $E > 0$ too. On the other hand, if $\xi = 0$, then (A.5) reduces to $(D\mathbf{d}) \cdot (E\mathbf{e}) = 0$. Since the real component $D\mathbf{d}$ is non-zero, this implies that either $E\mathbf{e} = 0$ (i.e. $E = 0$ and $D = \mu$) or $\mathbf{d}$ and $\mathbf{e}$ are perpendicular. In the latter case there are an infinite family of pairs (D, E) which satisfy (A.4). Without loss of generality we can, in this case, assume that $E > 0$ (we can multiply $\mathbf{e}$ by minus one if necessary).

To summarise, we have shown that if (A.3) is a solution of (A.1) then $\mathbf{d}, \mathbf{e}, D$ and E must satisfy (A.4)–(A.5) and without loss of generality we may assume that $D > 0$, $E \geqslant 0$, and $\mathbf{d} \cdot \mathbf{e} \geqslant 0$. Under these assumptions, the wave (A.2) propagates in the direction of $\mathbf{d}$, while decaying in the direction $\mathbf{e}$; in fact, we note that D and E are interpreted by some authors as the real and imaginary parts of an "apparent refractive index" (cf. Chang et al. (2005); Yang & Liou (1995)).

A.2 *An interface between two media with arbitrary absorption*

We now consider the canonical problem of the reflection/refraction of an incident plane wave of the general form (A.3) propagating in a medium with refractive index $\mu_1 + \mathrm{i}\xi_1$ at a planar interface with a second medium with refractive index $\mu_2 + \mathrm{i}\xi_2$. We assume that in the first medium the field takes the form $u = u^i + u^r$, where u^i is the incident plane wave and u^r is a reflected plane wave, and that in the second medium the field takes the form $u = u^t$, where u^t is a transmitted plane wave. We also assume that both the total field u and its normal derivative are continuous across the interface, which implies that, on the interface,

$$u^i + u^r = u^t \quad \text{and} \quad \frac{\partial u^i}{\partial \mathbf{n}} + \frac{\partial u^r}{\partial \mathbf{n}} = \frac{\partial u^t}{\partial \mathbf{n}}, \tag{A.6}$$

where $\mathbf{n}$ is a vector normal to the interface. We write the waves u^i, u^r and u^t in the general form (A.3) as:

$$\begin{aligned}
u^i &= A^i \exp\{\mathrm{i}k_0(D_i\mathbf{d}^i + \mathrm{i}E_i\mathbf{e}^i)\cdot\mathbf{x}\}, \\
u^r &= A^r \exp\{\mathrm{i}k_0(D_i\mathbf{d}^r + \mathrm{i}E_i\mathbf{e}^r)\cdot\mathbf{x}\}, \\
u^t &= A^t \exp\{\mathrm{i}k_0(D_t\mathbf{d}^t + \mathrm{i}E_t\mathbf{e}^t)\cdot\mathbf{x}\},
\end{aligned} \tag{A.7}$$

where we have assumed a priori the same "apparent refractive index" for the reflected wave as for the incident wave. Given the parameters A^i, $\mathbf{d}^i$, $\mathbf{e}^i$, D_i and E_i describing the incident wave, we wish to determine the parameters A^r, A^t, $\mathbf{d}^r$, $\mathbf{e}^r$, $\mathbf{d}^t$, $\mathbf{e}^t$, D_t and E_t determining the reflected and transmitted waves.

The geometry of the problem is illustrated in Figure 10. The real and imaginary components of the direction vectors have been drawn on separate diagrams for clarity, but it should be kept in mind that the complex incident direction vector is $\mathbf{d}^i + \mathrm{i}\mathbf{e}^i$ and that the reflected and transmitted direction vectors are $\mathbf{d}^r + \mathrm{i}\mathbf{e}^r$ and $\mathbf{d}^t + \mathrm{i}\mathbf{e}^t$, respectively.
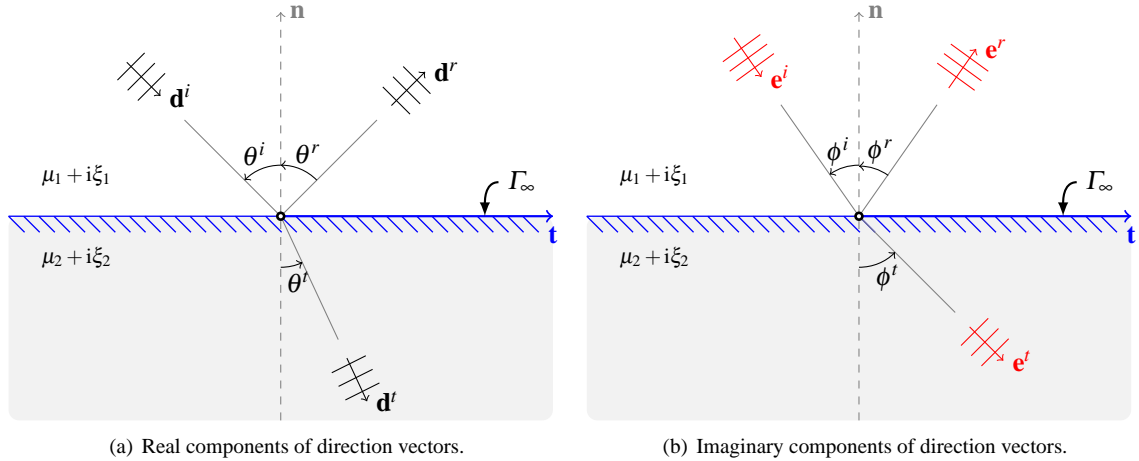

(a) Real components of direction vectors.   (b) Imaginary components of direction vectors.

FIG. 10: Refraction and reflection of light at the interface Γ_∞

A.2.1 The reflection law

We shall assume that the real and imaginary components of the incident and reflected direction vectors satisfy the *specular reflection law* ("angle of reflection equals angle of incidence"), which can be stated in vector notation as

$$\boxed{\begin{aligned}
\mathbf{d}^r &= \mathbf{d}^i - 2(\mathbf{d}^i \cdot \mathbf{n})\mathbf{n}, \\
\mathbf{e}^r &= \mathbf{e}^i - 2(\mathbf{e}^i \cdot \mathbf{n})\mathbf{n},
\end{aligned}} \tag{A.8}$$

or, in the notation of Figure 10, simply as

$$\theta^i = \theta^r, \quad \phi^i = \phi^r.$$

A.2.2 Snell's law and the Fresnel formulae

Snell's law relates the tangential components of the incident and transmitted direction vectors. The Fresnel formulae relate the amplitudes of the reflected and transmitted waves to that of the incident wave. To derive these relationships we first substitute the representations (A.7) into the boundary conditions (A.6). Eliminating $\mathbf{d}^r$ and $\mathbf{e}^r$ using the law of reflection (A.8) gives, for any $\mathbf{x} \in \Gamma_\infty$,

$$\left(A^i + A^r \exp\{-2\mathrm{i}k_0(D_i\mathbf{d}^i \cdot \mathbf{n} + E_i\mathbf{e}^i \cdot \mathbf{n})\mathbf{n} \cdot \mathbf{x}\}\right) \exp\{\mathrm{i}k_0(D_i\mathbf{d}^i + \mathrm{i}E_i\mathbf{e}^i) \cdot \mathbf{x}\} = A^t \exp\{\mathrm{i}k_0(D_t\mathbf{d}^t + \mathrm{i}E_t\mathbf{e}^t) \cdot \mathbf{x}\}, \quad \text{(A.9)}$$

and

$$v^i \left(A^i - A^r \exp\{-2\mathrm{i}k_0(D_i\mathbf{d}^i \cdot \mathbf{n} + E_i\mathbf{e}^i \cdot \mathbf{n})\mathbf{n} \cdot \mathbf{x}\}\right) \exp\{\mathrm{i}k_0(D_i\mathbf{d}^i + \mathrm{i}E_i\mathbf{e}^i) \cdot \mathbf{x}\} = v^t A^t \exp\{\mathrm{i}k_0(D_t\mathbf{d}^t + \mathrm{i}E_t\mathbf{e}^t) \cdot \mathbf{x}\},$$

$$\text{(A.10)}$$

where $v^i = D_i\mathbf{d}^i \cdot \mathbf{n} + \mathrm{i}E_i\mathbf{e}^i \cdot \mathbf{n}$ and $v^t = D_t\mathbf{d}^t \cdot \mathbf{n} + \mathrm{i}E_t\mathbf{e}^t \cdot \mathbf{n}$.

To derive Snell's law we write $\mathbf{x} \in \Gamma_\infty$ as

$$\mathbf{x} = \mathbf{X} + s\mathbf{t}, \quad \text{(A.11)}$$

where $\mathbf{X}$ is an arbitrary reference point on Γ_∞, $s \in \mathbb{R}$ and $\mathbf{t}$ is the unit tangent vector to Γ_∞ defined as $\mathbf{t} = (n_2, -n_1)$, where $\mathbf{n} = (n_1, n_2)$. Substituting (A.11) into (A.9) and rearranging gives

$$A^t = \exp\{\mathrm{i}k_0 s(D_i\mathbf{d}^i + \mathrm{i}E_i\mathbf{e}^i - D_t\mathbf{d}^t - \mathrm{i}E_t\mathbf{e}^t) \cdot \mathbf{t}\} \exp\{\mathrm{i}k_0(D_i\mathbf{d}^i + \mathrm{i}E_i\mathbf{e}^i - D_t\mathbf{d}^t - \mathrm{i}E_t\mathbf{e}^t) \cdot \mathbf{X}\}$$
$$\times \left(A^i + A^r \exp\{-2\mathrm{i}k_0(D_i\mathbf{d}^i + \mathrm{i}E_i\mathbf{e}^i \cdot \mathbf{n})\mathbf{n} \cdot \mathbf{X}\}\right). \quad \text{(A.12)}$$

Since this must hold for all $\mathbf{x} \in \Gamma_\infty$, i.e. for all $s \in \mathbb{R}$, the argument of the first exponential factor on the right-hand side must be equal to zero, i.e.

$$D_i\mathbf{d}^i \cdot \mathbf{t} + \mathrm{i}E_i\mathbf{e}^i \cdot \mathbf{t} - D_t\mathbf{d}^t \cdot \mathbf{t} - \mathrm{i}E_t\mathbf{e}^t \cdot \mathbf{t} = 0. \quad \text{(A.13)}$$

Comparing real and imaginary components of (A.13) then yields the vector form of *Snell's Law*:

$$\boxed{\begin{aligned} D_i\mathbf{d}^i \cdot \mathbf{t} &= D_t\mathbf{d}^t \cdot \mathbf{t}, \\ E_i\mathbf{e}^i \cdot \mathbf{t} &= E_t\mathbf{e}^t \cdot \mathbf{t}, \end{aligned}} \quad \text{(A.14)}$$

which can also be written in more classical form in terms of the notation of Figure 10 as

$$D_i \sin\theta^i = D_t \sin\theta^t, \qquad E_i \sin\phi^i = E_t \sin\phi^t.$$

To derive the Fresnel formulae, we note that, given the incident amplitude A^i, equations (A.9) and (A.10) are simultaneous equations in A^r and A^t which can be solved to give the reflection and transmission coefficients

$$\boxed{R := \frac{A^r}{A^i} = \frac{v_i - v_t}{v_i + v_t} \exp\{2\mathrm{i}k_0(D_i\mathbf{d}^i \cdot \mathbf{n} + \mathrm{i}E_i\mathbf{e}^i \cdot \mathbf{n})\mathbf{n} \cdot \mathbf{X}\},} \quad \text{(A.15)}$$

$$\boxed{T := \frac{A^t}{A^i} = \frac{2v_i}{v_i + v_t} \exp\{\mathrm{i}k_0(D_i\mathbf{d}^i + \mathrm{i}E_i\mathbf{e}^i - D_t\mathbf{d}^t - \mathrm{i}E_t\mathbf{e}^t) \cdot \mathbf{X}\},} \quad \text{(A.16)}$$

respectively, where, as above, $\mathbf{X}$ is an arbitrary reference point on Γ_∞. If the origin of our coordinate system lies on Γ_∞ then we may take $\mathbf{X} = \mathbf{0}$, giving

$$R = \frac{v_i - v_t}{v_i + v_t}, \qquad T = \frac{2v_i}{v_i + v_t},$$

along with the classical relationship $1 + R = T$.

A.2.3 Calculating D_t and E_t

We recall from §A.1 that D_t and E_t must satisfy the equations

$$D_t^2 - E_t^2 = \mu_2^2 - \xi_2^2, \tag{A.17}$$

$$D_t E_t \mathbf{d}^t \cdot \mathbf{e}^t = \mu_2 \xi_2. \tag{A.18}$$

Equation (A.18) can be written in terms of tangential and normal components as

$$D_t E_t [(\mathbf{d}^t \cdot \mathbf{t})(\mathbf{e}^t \cdot \mathbf{t}) + (\mathbf{d}^t \cdot \mathbf{n})(\mathbf{e}^t \cdot \mathbf{n})] = \mu_2 \xi_2. \tag{A.19}$$

After rearranging (A.19), squaring, and writing the normal components in terms of the tangential components (using the fact that $(\mathbf{d}^t \cdot \mathbf{t})^2 + (\mathbf{d}^t \cdot \mathbf{n})^2 = (\mathbf{e}^t \cdot \mathbf{t})^2 + (\mathbf{e}^t \cdot \mathbf{n})^2 = 1$), Snell's law implies that

$$(D_t^2 - \tilde{D}_i^2)(E_t^2 - \tilde{E}_i^2) = (\mu_2 \xi_2 - \tilde{D}_i \tilde{E}_i)^2,$$

where $\tilde{D}_i := D_i \mathbf{d}^i \cdot \mathbf{t}$ and $\tilde{E}_i := E_i \mathbf{e}^i \cdot \mathbf{t}$. Finally, using (A.17) to eliminate E_t, we arrive at a quadratic equation satisfied by D_t^2,

$$D_t^4 + D_t^2[\xi_2^2 - \mu_2^2 - \tilde{E}_i^2 - \tilde{D}_i^2] + \tilde{D}_i^2(\mu_2^2 - \xi_2^2) - (\mu_2 \xi_2)^2 + 2\mu_2 \xi_2 \tilde{D}_i \tilde{E}_i = 0, \tag{A.20}$$

and the quadratic formula yields the solutions of (A.20) as

$$D_t^2 = \frac{1}{2}\left(\mu_2^2 - \xi_2^2 + \tilde{D}_i^2 + \tilde{E}_i^2 \pm \sqrt{(\mu_2^2 - \xi_2^2 - \tilde{D}_i^2 + \tilde{E}_i^2)^2 + 4(\tilde{D}_i \tilde{E}_i - \mu_2 \xi_2)^2}\right). \tag{A.21}$$

Similar equations have been derived in Chang et al. (2005) and Yang & Liou (1995); however, the correct sign to choose in (A.21) is not discussed in these references. We claim that the positive square root should be taken in (A.21) for consistency with Snell's law. To justify this statement, we note that Snell's law trivially implies the inequalities

$$D_t^2 \geqslant \tilde{D}_i^2, \tag{A.22}$$

$$E_t^2 \geqslant \tilde{E}_i^2. \tag{A.23}$$

We can rearrange (A.21) to give

$$D_t^2 - \tilde{D}_i^2 = \frac{1}{2}(a \pm \sqrt{a^2 + b^2}), \tag{A.24}$$

$$E_t^2 - \tilde{E}_i^2 = \frac{1}{2}(-a \pm \sqrt{a^2 + b^2}), \tag{A.25}$$

where $a := \mu_2^2 - \xi_2^2 - \tilde{D}_i^2 + \tilde{E}_i^2$ and $b := 2(\tilde{D}_i \tilde{E}_i - \mu_2 \xi_2)$. Then if $a < 0$, it is clear from (A.24) that we must take the positive square root in order to satisfy (A.22). If $a > 0$, it is clear from (A.25) that we must take the positive square root in order to satisfy (A.23). If $a = 0$, then we must take the positive square root in order to satisfy both (A.22) and (A.23), unless of course $b = 0$ too, in which case the sign choice is immaterial.

Having justitifed the choice of the positive square root in (A.21), we can state the formulae for D_t and E_t:

$$
D_t = \sqrt{\frac{1}{2}\left(\mu_2^2 - \xi_2^2 + \tilde{D}_i^2 + \tilde{E}_i^2 + \sqrt{(\mu_2^2 - \xi_2^2 - \tilde{D}_i^2 + \tilde{E}_i^2)^2 + 4(\tilde{D}_i\tilde{E}_i - \mu_2\xi_2)^2}\right)},
$$
$$
E_t = \sqrt{D_t^2 + \xi_2^2 - \mu_2^2},
$$

(A.26)

where the non-negative square root is taken in both equations.

A.2.4 Normal components of transmitted direction vectors

Snell's law provides a formula for the tangential components of the transmitted direction vectors $\mathbf{d}^t$ and $\mathbf{e}^t$. The fact that $\mathbf{d}^t$ and $\mathbf{e}^t$ are unit vectors allows us to write

$$
\mathbf{d}^t = (\mathbf{d}^t \cdot \mathbf{t})\mathbf{t} + (\mathbf{d}^t \cdot \mathbf{n})\mathbf{n} = (\mathbf{d}^t \cdot \mathbf{t})\mathbf{t} \pm \sqrt{1 - (\mathbf{d}^t \cdot \mathbf{t})^2}\mathbf{n},
$$

(A.27)

$$
\mathbf{e}^t = (\mathbf{e}^t \cdot \mathbf{t})\mathbf{t} + (\mathbf{e}^t \cdot \mathbf{n})\mathbf{n} = (\mathbf{e}^t \cdot \mathbf{t})\mathbf{t} \pm \sqrt{1 - (\mathbf{e}^t \cdot \mathbf{t})^2}\mathbf{n},
$$

(A.28)

so that the normal components are specified up to sign. The need to make a sign choice in (A.27) and (A.28) is alluded to in Dupertuis et al. (1994, p. 1163), but a clear prescription of which sign to take is not provided there. We now provide such a presciption based on physical considerations. We note that a similar justification has been given in Pincherle (1947), but that this work does not appear to be widely known.

We consider first $\mathbf{d}^t$. The physically correct sign choice in (A.27) is made by considering the energy flow across the interface. The time-averaged intensity of a time-harmonic wave associated with a solution u of the Helmholtz equation (A.1) is given by $\langle\mathbf{I}\rangle = C\mathrm{Im}\,[\bar{u}\nabla u]$, where C is a positive constant depending on the frequency (cf. e.g. (Hewett, 2010, §3.4.2)). When u is a plane wave of the form (A.3) this gives $\langle\mathbf{I}\rangle = C|A|^2 k_0 D\mathbf{d}$, so that the energy flow is purely in the real propagation direction $\mathbf{d}$. In the context of the interface problem there are three cases to consider:

- When both $|\mathbf{d}^i \cdot \mathbf{t}| < 1$ and $|\mathbf{d}^t \cdot \mathbf{t}| < 1$ (so that $\mathbf{d}^i \cdot \mathbf{n} \neq 0$ and $\mathbf{d}^t \cdot \mathbf{n} \neq 0$) we stipulate that the time-averaged intensities $\langle\mathbf{I}_i\rangle$ and $\langle\mathbf{I}_t\rangle$ associated with the incident and transmitted waves should satisfy

$$
\mathrm{sgn}(\langle\mathbf{I}_i\rangle \cdot \mathbf{n}) = \mathrm{sgn}(\langle\mathbf{I}_t\rangle \cdot \mathbf{n}),
$$

to ensure that the transmission process preserves the direction of energy flow relative to the boundary. By the above discussion this means that we require

$$
\mathrm{sgn}(\mathbf{d}^t \cdot \mathbf{n}) = \mathrm{sgn}(\mathbf{d}^i \cdot \mathbf{n}),
$$

so that (A.27) becomes, after applying Snell's law,

$$
\mathbf{d}^t = \frac{D_i}{D_t}(\mathbf{d}^i \cdot \mathbf{t})\mathbf{t} + \mathrm{sgn}(\mathbf{d}^i \cdot \mathbf{n})\sqrt{1 - \left(\frac{D_i}{D_t}\right)^2(\mathbf{d}^i \cdot \mathbf{t})^2}\mathbf{n}.
$$

(A.29)

This formula implies that the transmitted wave is always propagating into the second medium, except for the case of total internal reflection which is discussed below.

- When $|\mathbf{d}^t \cdot \mathbf{t}| = 1$, we have that $\mathbf{d}^t \cdot \mathbf{n} = 0$ and there is no sign choice to be made. This case corresponds to the phenomenon of *total internal reflection* (TIR). The energy flow in the second medium in this case is parallel to the interface.

- When $|\mathbf{d}^i \cdot \mathbf{t}| = 1$ (i.e. $\mathbf{d}^i \cdot \mathbf{n} = 0$), we take $\mathbf{d}^t$ to point into the second medium. We note that if $E_i = 0$ then $v_i = 0$, and so $R = -1$ and $T = 0$ (i.e. the solution is identically zero).

We now turn to $\mathbf{e}^t$. It turns out that, having specified the sign choice in (A.27), the sign choice in (A.28) follows immediately. Indeed, provided that $E_t \mathbf{d}^t \cdot \mathbf{n} \neq 0$, $\mathbf{e}^t \cdot \mathbf{n}$ is now completely determined by (A.19), with

$$\mathbf{e}^t \cdot \mathbf{n} = \frac{1}{D_t E_t \mathbf{d}^t \cdot \mathbf{n}} \left(\mu_2 \xi_2 - D_i E_i (\mathbf{d}^i \cdot \mathbf{t})(\mathbf{e}^i \cdot \mathbf{t}) \right), \qquad E_t \mathbf{d}^t \cdot \mathbf{n} \neq 0.$$

Thus

$$\mathbf{e}^t = \frac{E_i}{E_t} (\mathbf{e}^i \cdot \mathbf{t}) \mathbf{t} + \frac{1}{D_t E_t \mathbf{d}^t \cdot \mathbf{n}} \left(\mu_2 \xi_2 - D_i E_i (\mathbf{d}^i \cdot \mathbf{t})(\mathbf{e}^i \cdot \mathbf{t}) \right) \mathbf{n}, \qquad E_t \mathbf{d}^t \cdot \mathbf{n} \neq 0. \tag{A.30}$$

This equation predicts that the vector $\mathbf{e}^t$ sometimes points back into the first (incident) medium. This somewhat counterintuitive behaviour was noted in Pincherle (1947); however, some subsequent authors (in particular, Chang et al. (2005)), seemingly unaware of Pincherle's work, artifically force $\mathbf{e}^t$ to point into the second medium, despite the fact that this may lead to a violation of the Helmholtz equation. We remark that a similar, artificial modification to the laws of reflection/refraction is made in Bi et al. (2011) and Yang & Liou (2009), where the transmitted wave is spuriously forced to be homogeneous, when in practice it could be inhomogeneous as outlined above.

When $E_t = 0$ or $\mathbf{d}^t \cdot \mathbf{n} = 0$ the formula (A.30) cannot be applied. The former case is easily dealt with: since E_t and $\mathbf{e}^t$ appear in a product in the formula (A.3), the choice of $\mathbf{e}^t$ is irrelevant when $E_t = 0$, and we may arbitrarily assign $\mathbf{e}^t = \mathbf{d}^t$, for example. The latter case $\mathbf{d}^t \cdot \mathbf{n} = 0$ corresponds to TIR, and in this case we argue that the transmitted wave should decay (not grow) with increasing distance from the interface, so that we require $\mathrm{sgn}(\mathbf{e}^t \cdot \mathbf{n}) = \mathrm{sgn}(\mathbf{d}^i \cdot \mathbf{n})$, giving

$$\mathbf{e}^t = \frac{E_i}{E_t} (\mathbf{e}^i \cdot \mathbf{t}) \mathbf{t} + \mathrm{sgn}(\mathbf{d}^i \cdot \mathbf{n}) \sqrt{1 - \left(\frac{E_i}{E_t} \right)^2 (\mathbf{e}^i \cdot \mathbf{t})^2} \mathbf{n}, \qquad \mathbf{d}^t \cdot \mathbf{n} = 0. \tag{A.31}$$

References

Y. Antipov & V. Silvestrov (2007). 'Diffraction of a plane wave by a right-angled penetrable wedge'. *Radio Sci.* **42**(4):RS4006.

X. Antoine & H. Barucq (2005). 'Approximation by generalised impedance boundary conditions of a transmission problem in acoustic scattering'. *ESAIM Math. Model. Numer. Anal.* **39**(5):1041–1059.

A. J. Baran (2012). 'From the single-scattering properties of ice crystals to climate prediction: A way forward'. *Atmos. Res.* **112**:45–69.

H. L. Bertoni, et al. (1978). 'Shadowing an inhomogeneous plane wave by an edge'. *J. Opt. Soc. Amer.* **68**(7):983–988.

L. Bi, et al. (2011). 'Scattering and absorption of light by ice particles: Solution by a new physical-geometric optics hybrid method'. *J. Quant. Spectrosc. Ra.* **112**:1492–1508.

M. Born & E. Wolf (1997). *Principles of Optics*. Cambridge University Press.

V. A. Borovikov & B. Y. Kinber (1994). *Geometrical Theory of Diffraction*. IEE.

J. J. Bowman, et al. (1969). *Electromagnetic and Acoustic Scattering by Simple Shapes*. North-Holland, Amsterdam.

L. M. Brekhovskikh (1960). *Waves in Layered Media*. Academic Press.

B. Budaev & D. Bogy (1999). 'Rigorous solutions of acoustic wave diffraction by penetrable wedges'. *J. Acoust. Soc. Am.* **105**:74.

S. N. Chandler-Wilde, et al. (2012a). 'Numerical-asymptotics boundary integral methods in high-frequency acoustic scattering'. *Acta Numer.* pp. 89–305.

S. N. Chandler-Wilde, et al. (2012b). 'A high frequency boundary element method for scattering by a class of nonconvex obstacles'. *Submitted for publication - University of Reading preprint MPS-2012-04* .

S. N. Chandler-Wilde & S. Langdon (2007). 'A Galerkin boundary element method for high frequency scattering by convex polygons'. *SIAM J. Numer. Anal.* **45**(2):610–640.

S. N. Chandler-Wilde, et al. (2012c). 'A high frequency boundary element method for scattering by convex polygons with impedance boundary conditions'. *Commun. Comput. Phys.* **11**(2):575–593.

P. C. Y. Chang, et al. (2005). 'Ray tracing in absorbing media'. *J. Quant. Spectrosc. Ra.* **96**:327–341.

D. Colton & R. Kress (1983). *Integral Equation Methods in Scattering Theory*. Wiley.

M. Costabel & E. Stephan (1985). 'A direct boundary integral equation method for transmission problems'. *J. Math. Anal. Appl.* **106**:367–413.

V. Domínguez, et al. (2008). 'Dirac delta methods for Helmholtz transmission problems'. *Adv. Comput. Math.* **28**(2):119–139.

M. A. Dupertuis, et al. (1994). 'Generalization of complex Snell-Descartes and Fresnel laws'. *J. Opt. Soc. Amer. A* **11**(3):1159–1166.

S. Groth (2011). 'Light scattering by penetrable convex polygons'. MSc thesis, University of Reading.

S. P. Groth, et al. (2013). 'A high frequency boundary element method for scattering by penetrable convex polygons'. In preparation.

H. Haddar, et al. (2005). 'Generalized impedance boundary conditions for scattering by strongly absorbing obstacles: The scalar case'. *Math. Mod. Meth. Appl. Sci.* **15**:1273–1300.

D. P. Hewett (2010). *Sound propagation in an urban environment*. DPhil thesis, University of Oxford.

D. P. Hewett, et al. (2012). 'A high frequency *hp* boundary element method for scattering by convex polygons'. *SIAM J. Numer. Anal., to appear (University of Reading preprint MPS-2011-18)* .

R. Hiptmair & C. Jerez-Hanckes (2012). 'Multiple traces boundary integral formulation for Helmholtz transmission problems'. *Adv. Comput. Math.* **37**:39–91.

G. C. Hsiao & L. Xu (2011). 'A system of boundary integral equations for the transmission problem in acoustics'. *Appl. Numer. Math.* **61**:1017–1029.

G. James (1986). *Geometrical Theory of Diffraction for Electromagnetic Waves*, vol. 1. Peter Peregrinus Ltd.

D. S. Jones (1964). *The Theory of Electromagnetism*. Macmillan.

J. B. Keller (1962). 'Geometrical theory of diffraction'. *J. Opt. Soc. Amer.* **52**(2):116–130.

A. Kleefeld (2012). 'The transmission problem for the Helmholtz equation in R^3'. *Comput. Methods Appl. Math.* **12**(3):330–350.

R. E. Kleinman & P. A. Martin (1988). 'On single integral equations for the transmission problem of acoustics'. *SIAM J. Appl. Math.* **48**(2):307–325.

R. Kress & G. F. Roach (1978). 'Transmission problems for the Helmholtz equation'. *J. Math. Phys.* **19**(6):1433–1437.

A. R. Laliena, et al. (2009). 'Symmetric boundary integral formulations for Helmholtz transmission problems'. *Appl. Numer. Math.* **59**:2814–2823.

A. Macke, et al. (1996). 'Single scattering properties of atmospheric ice crystals'. *J. Atmos. Sci.* **53**(19):2813–2825.

E. Marmolejo-Olea, et al. (2012). 'Transmission boundary problems for Dirac operators on Lipschitz domains and applications to Maxwell's and Helmholtz's equations'. *Trans. Amer. Math. Soc.* **364**(8):4369–4424.

E. Meister, et al. (1994). 'Two canonical wedge problems for the Helmholtz equation'. *Math. Methods Appl. Sci.* **17**:877–899.

F. W. J. Olver, et al. (eds.) (2010). *NIST Handbook of Mathematical Functions*. Cambridge University Press, New York, NY.

L. Pincherle (1947). 'Refraction of plane non-uniform electromagnetic waves between absorbing media'. *Physical Review* **72**(3):232.

M.-L. Rapún & F.-J. Sayas (2006). 'Indirect methods with Brakhage-Werner potentials for Helmholtz transmission problems'. In A. B. de Castro, D. Gómez, P. Quintela, & P. Salgado (eds.), *Numerical Mathematics and Advanced Applications*, pp. 1146–1154. Spring-Verlag, Berlin.

M.-L. Rapún & F.-J. Sayas (2008). 'Mixed boundary integral methods for Helmholtz transmission problems'. *J. Comput. Appl. Math.* **214**:238–258.

A. D. Rawlins (1999). 'Diffraction by, or diffusion into, a penetrable wedge'. *Proc. R. Soc. Lond. A* **455**:2655–2686.

R. H. Torres & G. V. Welland (1993). 'The Helmholtz equation and transmission problems with Lipschitz interfaces'. *Indiana Univ. Math. J.* **42**(4):1457–1486.

T. von Petersdorff (1989). 'Boundary integral equations for mixed Dirichlet, Neumann and transmission problems'. *Math. Methods Appl. Sci.* **11**:185–213.

P. Yang & K. N. Liou (1995). 'Light scattering by hexagonal ice crystals: comparison of finite-difference time domain and geometric optics models'. *J. Opt. Soc. Amer. A* **12**(1):162–176.

P. Yang & K. N. Liou (1996). 'Geometric-optics-integral-equations method for light scattering by nonspherical ice crystals'. *Appl. Optics* **35**(33):6568–6584.

P. Yang & K. N. Liou (1997). 'Light scattering by hexagonal ice crystals: solutions by a ray-by-ray integration algorithm'. *J. Opt. Soc. Amer. A* **14**(9):2278–2289.

P. Yang & K. N. Liou (2009). 'Effective refractive index for determining ray propagation in an absorbing dielectric particle'. *J. Quant. Spectrosc. Ra.* **110**:300–306.

A. Zinn (1989). 'A numerical method for transmission problems for the Helmholtz equation'. *Computing* **41**(3):267–274.